# Charles University

# Faculty of Science

Ph.D. program: Physical Chemistry



**Ghulam Abbas, M.Sc.**


# *In-situ* Raman Spectroelectrochemistry of Graphene and Related Materials in Concentrated Aqueous Electrolytes

**Doctoral thesis**

**Supervisor: Mgr. Otakar Frank Ph.D.**

Prague, 2022

The research work presented in this Doctoral thesis was financially supported by Czech Science Foundation (GACR Grant No. 19-23986S), European Regional Development Fund; OP RDE; Project: “Carbon allotropes with rationalized nanointerfaces and nanolinks for environmental and biomedical applications” (No. CZ.02.1.01/0.0/0.0/16_026/0008382), Charles University Grant Agency (GAUK, project No. 371621), and LTAUSA19001 by the Ministry of Education, Youth and Sports of the Czech Republic.

**Acknowledgements**

I would like to express my great thanks to my supervisor Dr. Otakar Frank and my consultants Dr. Matej Velický and Dr. Farjana J. Sonia for their kind guidance, patience and help. Also, I am thankful to all my colleagues of the Nanocarbon group at the J. Heyrovsky Institute of Physical Chemistry and to our collaborators from the Institute of Physics of the CAS. Finally, to my family and friends for their support that made it possible for me to complete my thesis.

**Abstrakt**

Vzájemná provázanost vlastností materiálu a elektrochemických procesů často probíhajících na jeho všudypřítomných okrajích ztěžuje rozlišení role jednotlivých defektů v procesech přenosu náboje v materiálu. Proto jsme použili in-situ μ-kapkovou Ramanovu spektroelektrochemii (SEC), abychom identifikovali procesy lokalizovaného přenosu náboje přes bazální rovinu a defekty v oblasti o velikosti 10-20 $\mu m^2$ v čistém a defektním jednovrstvém grafenu. Bylo zjištěno, že dva odlišné procesy přenosu elektronů s nižší a vyšší rychlostí existují vedle sebe ve stejném vzorku, ale jsou omezeny na oblasti bez defektů a na oblasti bohaté na defekty. Kromě toho, za účelem prozkoumání mechanismu elektrochemické interkalace iontů pro dobíjecí baterie, byla provedena in-situ Ramanova SEC v makro elektrochemické cele. Bylo pozorováno, že strukturní vlastnosti, jako je velikost laterální domény ($L_a$), stupeň grafitizace ($g$), vzdálenost mezi defekty ($L_D$) a hustota defektů ($n_D$), mají podstatný vliv na elektrochemickou (de)interkalaci aniontu do přírodního a kish grafitu během nabíjecích/vybíjecích procesů. Bylo také zjištěno, že ultrazvuková úprava přírodního grafitu snižuje $L_a$, což zvyšuje reverzibilitu aniontové (de)interkalace v koncentrované vodném roztoku elektrolytu. Reverzibilitu aniontové (de)interkalace do vysoce orientovaného pyrolytického grafitu během procesu vybíjení prokázala také in-situ Ramanova SEC v elektrolytu typu „voda v soli“.

**Klíčová slova**: Ramanova spektroskopie, grafen, grafit, *in situ* Ramanova spektroelektrochemie, koncentrované elektrolyty.

**Abstract**

The complex interplay between the material's properties and the electrochemical process often taking place at its ubiquitous edges makes it difficult to discriminate the role of single defects in the charge transfer processes in the material. Therefore, we have performed *in-situ* μ-droplet Raman spectroelectrochemistry (SEC) to identify the localized charge transfer processes through the basal plane and defects in a selected localized area of 10-20 $\mu m^2$ of defect-free and defective monolayer graphene. It is noticed that two distinctive electron transfer processes of slower and faster rates exist side-by-side in the same sample but they are confined in the defect-free and defect-rich regions, respectively. Furthermore, in order to explore the electrochemical ion intercalation mechanism for rechargeable batteries, *in-situ* Raman SEC in a macro SEC cell was performed. It was observed that structural properties such as the lateral domain size ($L_a$), degree of graphitization ($g$), inter-defect distance ($L_D$) and defect density ($n_D$) have substantial influence on the electrochemical (de)intercalation of anion into natural and kish graphite during charge/discharge process. It was also revealed that ultrasound treatment of natural graphite reduces the $L_a$ which enhances the reversibility of the anion (de)intercalation in a concentrated aqueous electrolyte solution. The reversibility of anion (de)intercalation into highly oriented pyrolytic graphite during discharge process was also evidenced by *in-situ* Raman SEC using water-in-salt electrolyte.

**Key words**: Raman spectroscopy, graphene, graphite, *in situ* Raman spectroelectrochemistry, concentrated electrolytes.

## Table of Contents

# 1 Introduction

With its tremendous electronic properties, high thermal conductivity, charge carrier mobility, and mechanical properties, graphene is emerging as a serious contender for nanoelectronics and energy storage applications [1]. Raman spectroscopy, due to its nondestructive nature, is one of the most preferred characterization techniques for graphene and related carbon-based materials. It can provide information about the interfacial phenomena, doping, interlayer coupling, structural defects, and chemical functionalization [2].

As will be mentioned in detail in Chapter 2, the main objective of the present research work was to study *in-situ* Raman SEC of graphene and related materials using concentrated aqueous electrolytes in micro and macroscale. In Chapter 1, the fundamentals of graphene, its charge doping, defects and characterization by Raman spectroscopy will be explained first. In addition, *in-situ* Raman spectroscopy combined with the electrochemical technique called μ-droplet Raman SEC will be discussed. It allows to explore the doping-induced charge transfer process through the basal plane and defects in electrochemically top-gated graphene using the concentrated aqueous electrolyte. Furthermore, the reversibility of (de)intercalation of ions into graphite during the charge/discharge process using concentrated aqueous electrolytes and its understanding by *in-situ* Raman SEC at macroscale will also be discussed.

## 1.1 Graphene and related materials

Graphene is a one-atom thin, two-dimensional material (2DM) with a single layer of carbon atoms arranged in a honeycomb-like hexagonal structure [3]. It has a delocalized bond from the $2p_y$ orbital arranged out of plane and a σ bond (C-C) from the 2s and $2p_x$ orbitals arranged in plane [4,5]. The unit cell of a graphene single layer, defined by unit vectors $a_1$ and $a_2$, consists of two

carbon atoms, termed A and B, with the C-C bond distance of 0.142 nm. The honeycomb single layered structure of graphene is called the mother of all the carbon based materials [6]. The structure of graphite forms by stacking the graphene single layers along the *c*-axis in AB (or so-called Bernal) order, where the atoms in one layer are placed in the center of the hexagons of the two neighboring layers; graphite with AB stacking contains a unit cell with four carbon atoms [7]. The other stacking order in graphite is ABC [8]. The structure of graphene, graphite, and their unit cells are shown in Figure 1.

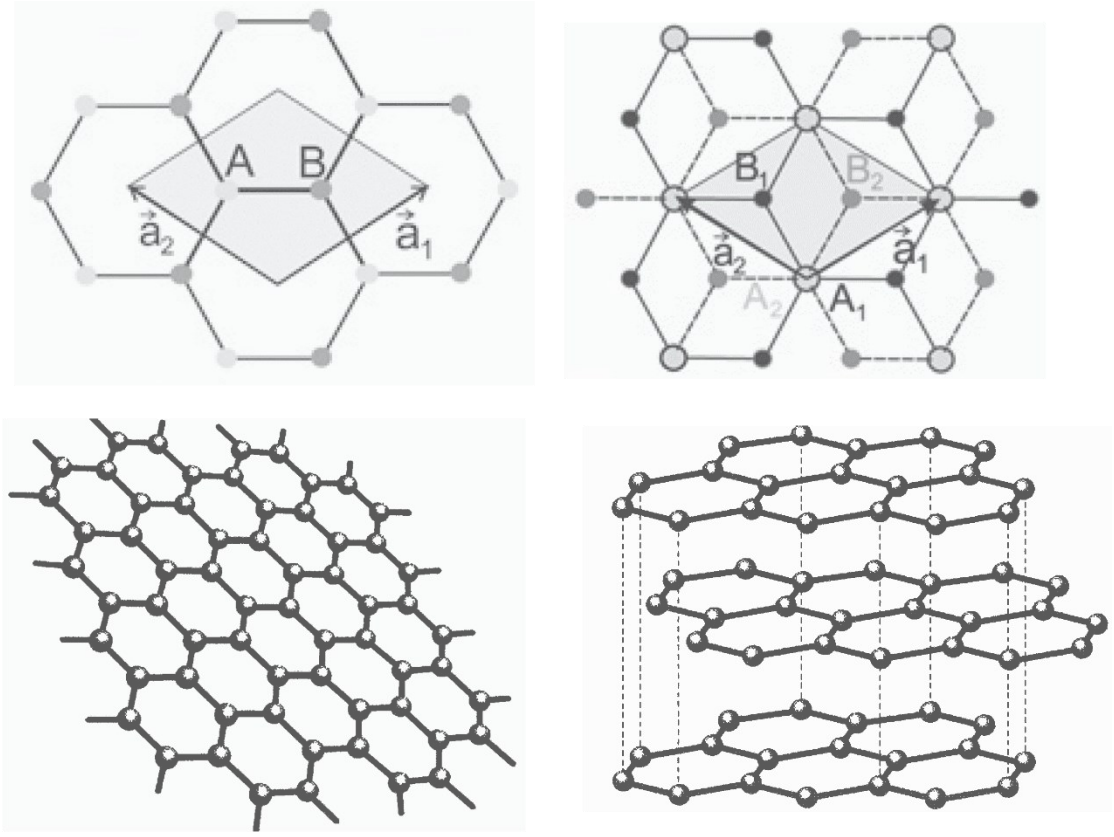


**Figure 1**: Structure of graphene and graphite; top: left, unit cell of single layer graphene, right, unit cell of multilayer graphene; bottom: right, structure of graphene, left, structure of graphite. Top picture was adapted with permission from Elsevier-Physics reports [7], bottom picture was reprinted by permission from IOP science, Physics World [6].

### 1.1.1 Preparation of graphene and its transfer techniques

The mechanical exfoliation of graphite using scotch tape, as shown in Figure 2, is the most common way to prepare the high-quality monolayers of graphene [9] but has limited scalability.

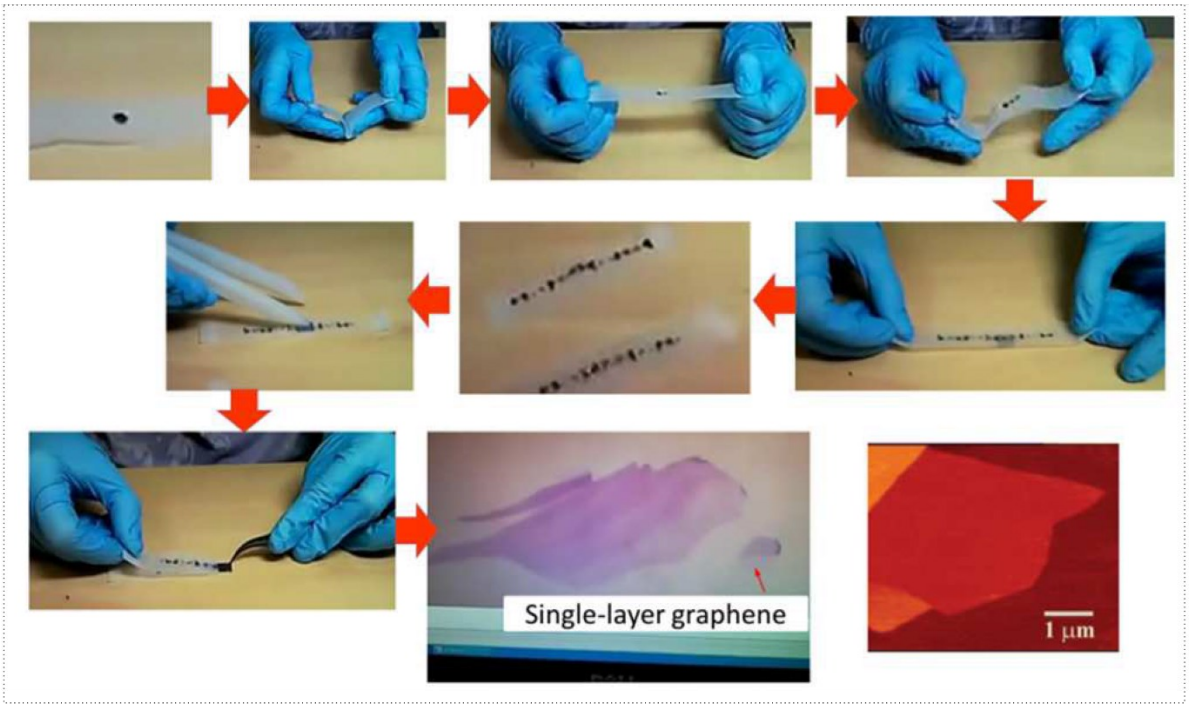


**Figure 2:** Preparation of graphene by the mechanical exfoliation of graphite. Adapted with permission from Royal Society of Chemistry [10].

The chemical and electrochemical exfoliation of graphite can produce large-scale graphene, but the quality is still questionable [11]. Although, the absolute yield is lower in chemical vapor deposition (CVD) method (still much higher than in mechanical exfoliation and it has been commercialized as well), it is capable of producing better quality graphene (but usually more defective than mechanical exfoliation). For a typical CVD growth of graphene, the methane is used as the carbon source that reacts with the catalytic metal substrate (e.g., nickel or copper) in the presence of hydrogen gas at a temperature around 1000 °C. Prior to the growth of graphene, the

metal is pre-treated with hydrogen gas to improve its quality. After the graphene growth is completed, the furnace is cooled down to room temperature [12,13].

Furthermore, the graphene grown on a metallic substrate cannot be directly used in most applications. Therefore, graphene is transferred to the commonly used $Si/SiO_2$ substrate or any other substrate of interest. Several methods have been utilized for transferring graphene. The most common one is a polymer—e.g., polymethyl methacrylate (PMMA)—assisted transfer [14]. However, due to contamination from the residues of the polymer, cellulose-assisted transfer has been adopted by many research groups [15]. In brief, PMMA or nitrocellulose is spin-coated on the graphene and then the metal substrate is dissolved in an appropriate etchant solution (iron (III) chloride solution is used as Cu etchant), which results in the graphene floating on the etchant solution. The graphene is scooped up ("fished") by the target substrate of and the polymer is removed after rinsing with acetone/methanol/isopropanol. The transfer technique is demonstrated schematically in Figure 3.

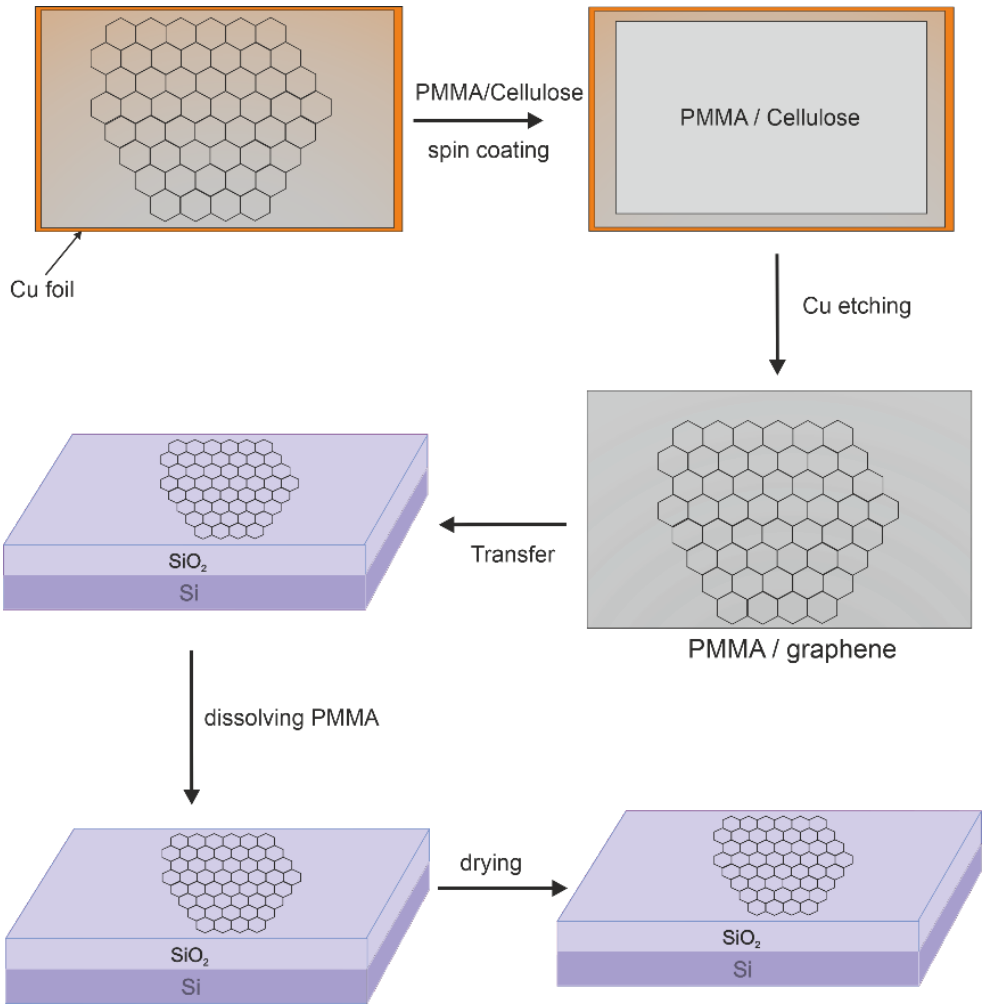


**Figure 3:** Transfer of CVD graphene from Cu onto $Si/SiO_2$ substrate.

### 1.1.2 Electronic band structure of graphene

As shown in Figure 4, the symmetry between the two sublattices A and B in a unit cell of graphene results in degeneracy between the conduction and valence bands at the K and K' points of the Brillouin zone (BZ) [16]. The degeneracy gives rise to the linear dispersion of mobile π electrons in the electronic bands of graphene [17-19]. The linear relationship of dispersion in graphene at the K point reveals that the charge carriers in graphene are massless Dirac fermions and have the

Fermi velocity ($V_F$) of $\approx 10^8$ cm $s^{-1}$ [20]. In the band structure of semimetal graphene, the conduction and valence band touch at the K point called the Dirac point [21]. Due to the interaction of graphene with foreign species, its Femi level changes which causes doping in graphene [22]. The energy changes around Γ symmetry point lead to the change in density of state (DOS). The unit cell in a single BZ of graphene, energy dispersion along the symmetry point, and the π band structure is represented in Figure 4.

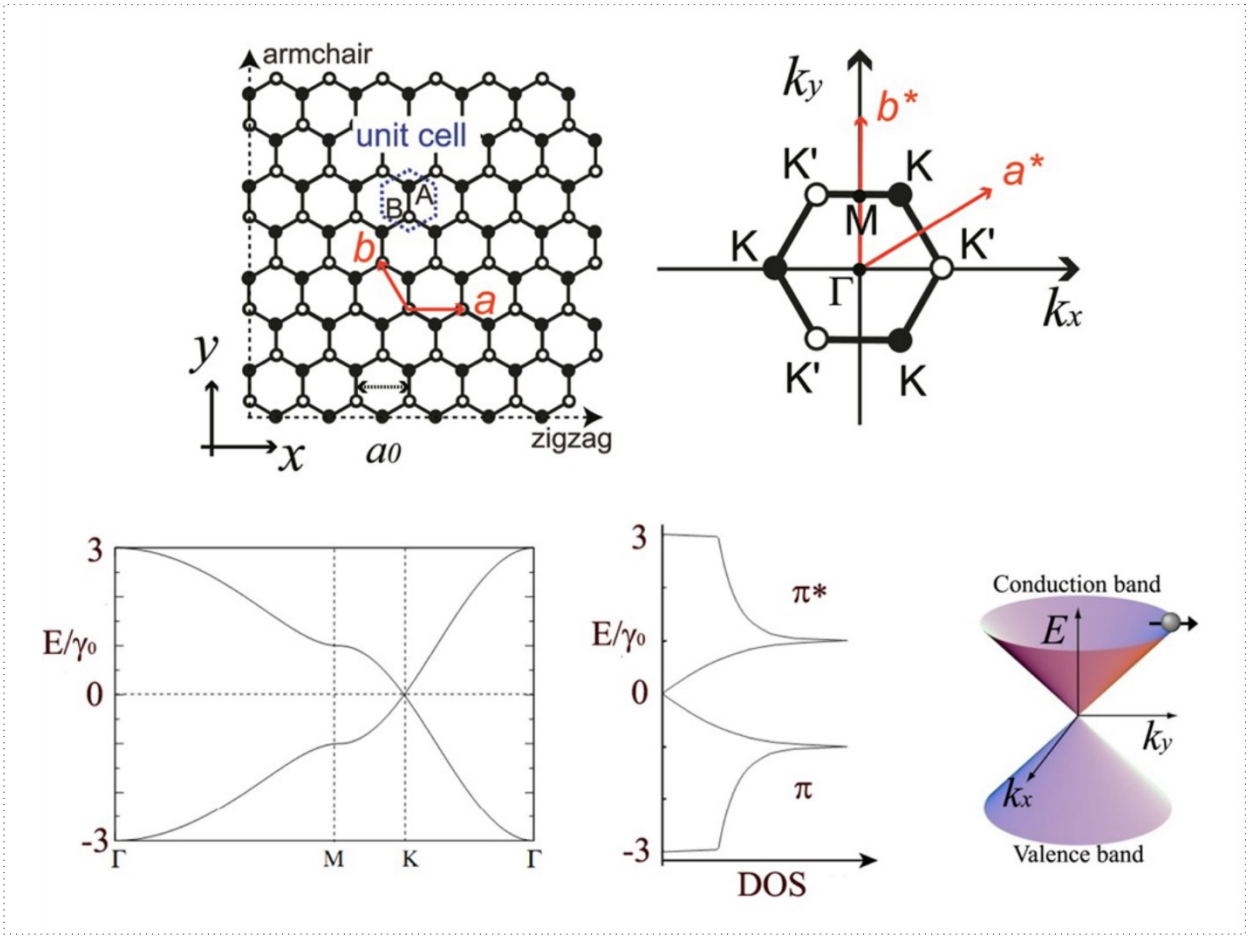


**Figure 4**: Top: left, graphene lattice structure in real space with basis vectors a and b; right, the reciprocal lattice vectors along with symmetry points (K, K', M and Γ) in the first Brillouin zone. Bottom: left, π-band structure of graphene along K, K', M, and Γ symmetry points in BZ. Middle, density of states for the π band. Right, π band structure of graphene near the K point. Reprinted with permission from American Chemical Society [21].

## 1.2 Raman spectroscopy of graphene and related materials

Raman spectroscopy is an efficient tool to characterize $sp^2$ carbon in graphene and related carbon materials [2,7,23]. It does not only reveal the structural and vibrational properties but also depicts their electronic properties. In addition, it also gives valuable information about the interfacial phenomena, electrochemical doping, interlayer coupling, structural defects and chemical functionalization [24–29]. The Raman spectra of $sp^2$ carbon-containing materials is very hard to interpret without understanding of the phonon dispersions [7]. Depending upon the direction of vibrations of the nearest C-C atoms that are perpendicular or parallel, phonon modes are categorized as longitudinal (L) and transverse (T) along the high symmetry ΓM and ΓK directions [7]. The monolayer of graphene consists of six phonon branches (iTA, iLA, oTO, oTA, iTO, iLO) in a unit cell of two carbon atoms. Among these, three are optical (O) and three are acoustic (A) branches of phonon dispersion. Two branches (one acoustic and one optic) are out of plane (o) and their atomic vibrations are perpendicular to the graphene plane. The remaining four, two acoustic and two optical, are in plane (i), with atomic vibrations parallel to the graphene plane [7,30]. The theoretically calculated phonon dispersion along the symmetry points is shown in Figure 5.

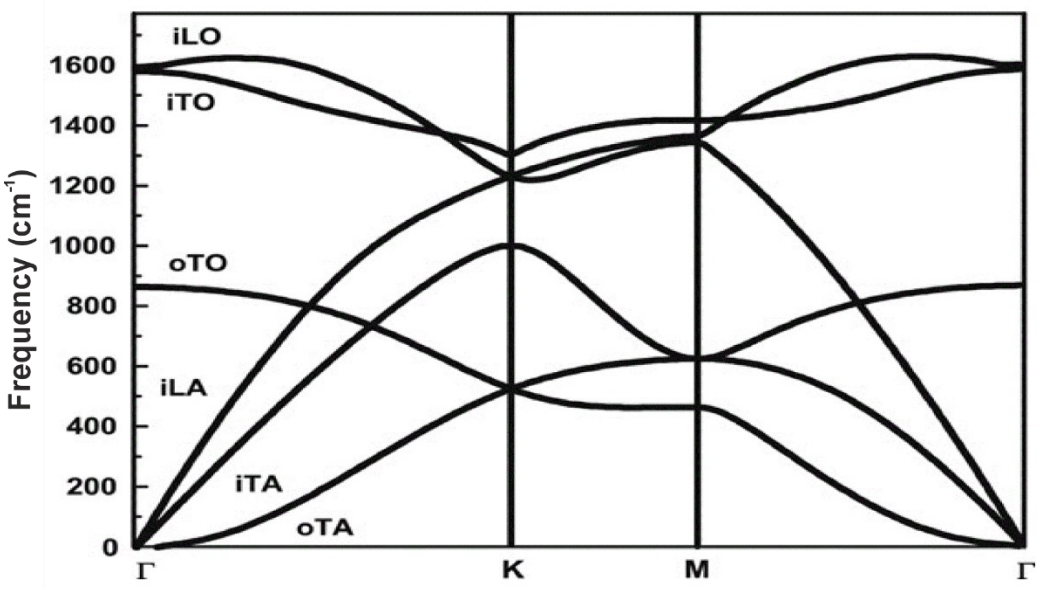


**Figure 5:** The calculated phonon dispersion for graphene. Printed with permission from American Physical Society [30].

The G band at 1582 $cm^{-1}$ (for suspended graphene) and the 2D band at 2500–2700 $cm^{-1}$ are the prominent signatures of the Raman spectrum of carbon $sp^2$ materials [2,31]. The G band is the outcome of a first order Raman scattering process with a doubly degenerate phonon (iTO, LO) mode of $E_{2g}$ symmetry at the Γ point. The 2D mode, which is also called G', originates from the second order Raman scattering process and is the outcome of two iTO phonons with opposite momenta near the K point. The strong disorder-induced D band at 1350 $cm^{-1}$ and the weak disorder-induced D' band at 1620 $cm^{-1}$ are the features, which enable the quantification of defects in the crystal lattice of graphene and related carbon based materials [28,32]. The D band is also a second order resonance process with one iTO phonon and one defect. The intensity difference of G to 2D band differentiates between monolayer and multilayer graphene (graphite) [33]. The Raman spectra of monolayer graphene and graphite are shown in Figure 6.

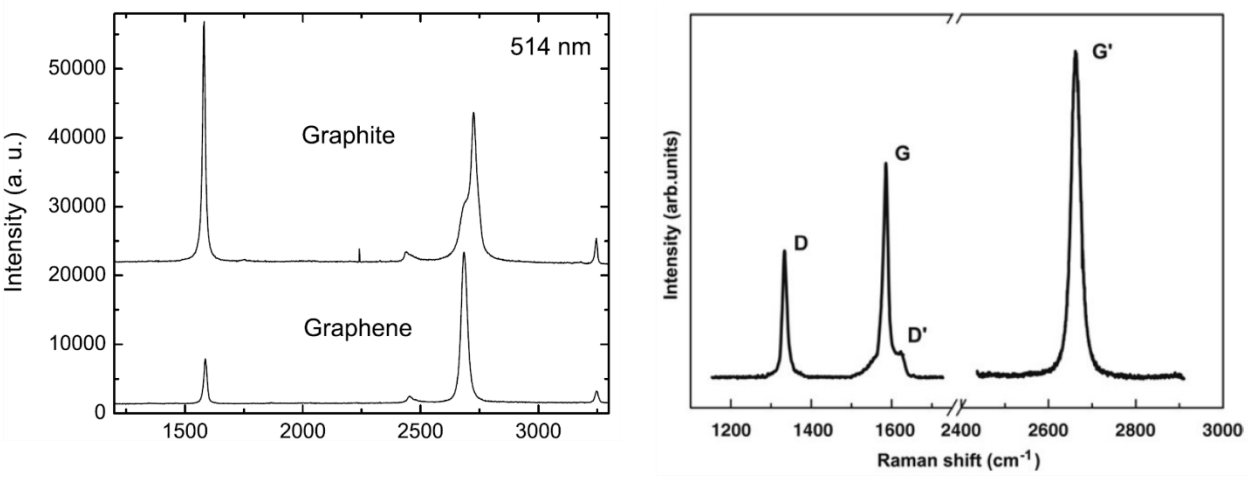


**Figure 6**: Left: Raman spectra of graphene and graphite. Adapted with permission from Elsevier [23]. Right, Raman spectrum of graphene showing defect-induced D and D' modes in graphene in addition to the G and 2D modes. Adapted with permission from Elsevier [7].

The interactions of photon with specific vibrations of a crystal lattice/molecule excites it to a virtual state with specific energy. In case of de-excitation, if the released energy is the same as the incoming photon energy, the scattering process is elastic and called Rayleigh scattering. The difference in energy of initial and outgoing photons in the case of inelastic scattering is the Raman shift (Stokes and anti-Stokes) which appears as bands in Raman signal. The Raman spectra of $sp^2$ carbon materials are always resonant due to the delocalization of π electrons, which enables to monitor their electronic as well as vibrational properties [34]. The intensity of the Raman peak in $sp^2$ graphene is significantly enhanced (~1000 times) due to the resonance effect caused by electron-phonon coupling [31,35]. The schematic illustration for the resonance Raman scattering processes of G, D, and 2D bands is demonstrated in Figure 7.

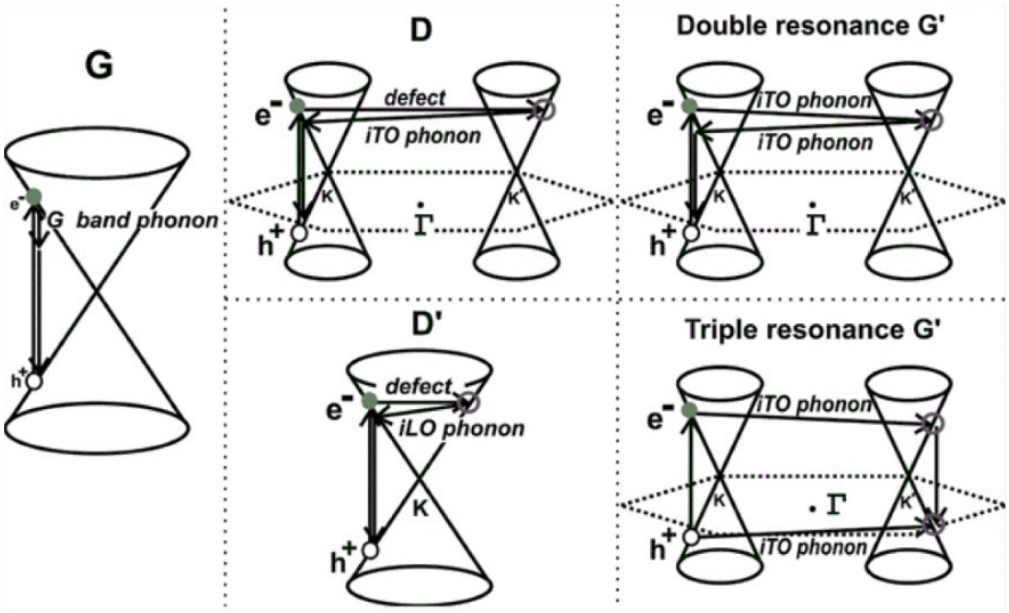


**Figure 7:** The resonance Raman scattering processes for the G, D, and 2D bands in graphene and related materials. Adapted with permission from Elsevier [36].

## 1.3 The characterization of doping and defects in graphene by Raman spectroscopy

Raman spectroscopy is one of the most preferred methods that can be helpful to monitor the charge doping in graphene [37,38]. The shift in G and 2D band frequency corresponds quantitatively to the change in charge carrier concentration. However, it is necessary to discriminate these effects from lattice deformation [39]. The precise evaluation of the Raman G peak frequency during the electrochemical doping allows us to determine the charge neutrality point (CNP) and to calculate the real charge carrier concentration in the material. The CNP could in fact be shifted from the "zero charge" position due to electrostatic effects or Coulombic screenings of ions at the graphene's surface [40,41]. Additionally, the underlying substrate (e.g., $Si/SiO_2$) is also known for inducing charge transfer to the material; however, the magnitude of the

charge varies with a particular substrate and environmental conditions such as humidity and temperature [42–44].

The quantification of the defects by Raman spectroscopy helps to get insights into the structural and electronic properties of graphene and its related materials [45,46]. The disorder induced in the crystal lattice, presented by defects, results in changing the lattice parameters and can be evaluated by the ratio of the D and G mode intensities ($I_D/I_G$) [45]. The $I_D/I_G$ can be used to calculate the structural parameters such as inter-defect distance ($L_D$), defect density ($n_D$), and crystallite domain size ($L_a$) following the formulas as reported in the literature [47–49].

### 1.4 Role of defects in the charge transfer processes in graphene

It is well known that structural defects play a decisive role in the charge transfer in graphene and its related materials and they alter the material's electronic properties [50]. The defects induced in the graphene structure lead to the change in its thermal conductivity and mechanical strength of graphene due to structural instabilities and changes in bond lengths [51]. The phenomenon of charge doping is localized [52,53]. The discrimination of the localized charge transfer process through edges/defects and defect-free basal region, on the other hand, is a complex issue that has not been fully discriminated in previous research. The electrochemical activity at the defects is order of magnitude higher compared with the defect-free basal plane. Hence, the electrochemistry in large-volume cells does not allow to discriminate the signals stemming from defects and basal plane/electrolyte interface. The most of the *in-situ* Raman SEC studies were conducted in the standard way at non-localized area using a large volume of the electrolyte covering the entire sheet of electrode [54–56]. Hence, it does not allow to get the precise information about the influence of localized defects on doping-induced changes in the Raman spectra.

A newly developed μ-droplet *in-situ* Raman SEC has been demonstrated to be an effective technique for obtaining precise information about the charge transfer process through defects and the basal plane in a localized area, as reported in our published work [57] and discussed in details in section 3.1. It can provide precise and facile electrochemical and spectroscopic characterization of the graphene with a spatial targeting area of the flake at a microscale.

### 1.5 *In-situ* Raman SEC and ionic intercalation mechanism in rechargeable batteries

In contrast, as the second objective of the current thesis is to study the ionic intercalation in graphite-based rechargeable batteries, i.e. on a bulk material, a macroscale *in-situ* Raman SEC was used for this purpose. One of the main anion storage mechanisms in rechargeable batteries is the electrochemical intercalation into layered materials [58]. Graphite, one of the most studied electrode materials for batteries and supercapacitors, manifests the formation of graphite intercalation compounds (GICs) where both cations and anions can enter the graphite's interlayer galleries [59]. GICs can be formed using metal cations, such as $Li^+$, $Na^+$, $K^+$, $Zn^{2+}$, $Al^{3+}$, and anions like bis(trifloromethanesulfonyl) imide ($TFSI^-$), hexafluorophosphate ($PF_6^-$), tetrafluoroborate ($BF_4^-$), tetrachloroaluminate ($AlCl_4^-$), or perchlorate ($ClO_4^-$) [60–67]. Even though graphite-based dual ion batteries (DIBs) with ionic liquid and organic electrolytes are promising in terms of stable and reversible electrochemical performance, they have demerit points, such as flammability, high cost, environmental issues, or unsuitability for an open-air environment. These issues severely hinder their applicability across a wide variety of technological fields [68,69].

Aqueous electrolytes can potentially overcome the issues of organic and ionic liquid electrolytes in DIBs due to their inherent nonflammability, high ionic conductivity, and they are easy-to-handle in an open-air environment [70,71]. However, aqueous electrolytes suffer from small

electrochemical potential window, limited by the difference in overpotentials for hydrogen and oxygen evolution reactions (~1.23V) [72]. Highly concentrated aqueous electrolytes have recently enabled enlargement of the electrochemical potential window by suppressing free water content and reducing electrolyte decomposition [73]. Increased salt concentration in aqueous electrolytes has also allowed the formation of lower-stage GICs as well as improved reversibility of ionic (de) intercalation [74]. Highly concentrated $Al(ClO_4)_3$ and $Zn(ClO_4)_2$ aqueous electrolytes with an electrochemical window in the range of 3—4 V and facile intercalation of $ClO_4^-$ anion in graphite have been reported to have the highest electrochemical stability [66,74].

The size, type, and even concentration of the intercalating species as well as the structure of graphite, influence the physiochemical properties of GICs [75]. However, structural properties of graphite also have a substantial influence on the electrochemical (de)intercalation of anionic species during the charge/discharge process [76]. The chemical exfoliation and ultrasound treatment of graphite induce the formation of defects in the lattice structure and reduce the crystallite size [77–79]. The small crystallite lateral domain size ($L_a$) enhances the ionic transport kinetics, which, in turn, improves the reversibility during electrochemical (dis)charge process [80]. The role of $L_a$ and the degree of graphitization ($g$) on anion intercalation in graphite has also been reported by Heckmann *et al*. [81] as well as in our published work [76].

Generally, cyclic voltammetry (CV) is performed to monitor the reversibility of the intercalation process. However, in order to gain deeper insights into electrochemical ionic intercalation and to understand its correlation with the incurred structural modifications, various *in-situ* studies such as X-ray photoelectron spectroscopy (XPS), transmission electron microscopy (TEM), or X-ray diffraction (XRD) and Raman spectroscopy combining with electrochemical measurements are

required [82,83]. Ostwald *et al.* performed *in-situ* XPS to investigate the surface evolution of a graphite electrode material during the intercalation process in a Li-ion battery [84]. However, due to depth limitations, *in-situ* XPS can only provide information about the first few nanometers from the surface of the material. TEM can provide atomically resolved pictures of the insertion/extraction process of the reactive ion [85], but the experiments are extremely demanding and cannot be routinely performed.

Therefore, *in-situ* Raman SEC and *operando* XRD are the most prominent tools that have been utilized to explore the structural changes during the ion storage mechanism [86,87]. *Operando* XRD reveals the lattice changes (contraction/expansion) in bulk during the electrochemical ionic intercalation process. The *operando* XRD can be complemented by the more surface-sensitive, *in-situ* Raman SEC, to provide information from the first tens to hundreds of nanometers depending on the studied material. It can also provide information about the reversibility of the charge/discharge process and the disorder induced in the material [74,76].

# 2 Aims and objectives

The present research work has been aimed at micro and macroscale *in-situ* Raman SEC of graphene and related materials using concentrated aqueous electrolytes, as the continuation of the previous research work of Dr. Otakar Frank and his research group at the J. Heyrovsky Institute of Physical Chemistry. In view of the broad area of studies, there are two strong components in the current research work: (i) the charge transfer processes in defect free areas (i.e., basal plane) and through defective regions (i.e., defects/edges) were discriminated by *in-situ* Raman SEC setup in a microelectrochemical cell at a selected area and (ii) the electrochemical ionic intercalation into graphite for rechargeable (Al and dual ion) batteries was explored by *in-situ* Raman SEC at macroscale. Hence the results and the discussion part of the thesis has been summarized concisely into two major sections, as follows.

# 3 Results and Discussion (concise summary)

## 3.1 Localized *in-situ* Raman SEC of graphene in a µ-droplet

As stated in section 1.4, it is difficult to discriminate charge transfer process through defect-free and defect-rich regions of graphene due to the ubiquitous edges (i.e., defects of a certain kind) in the commonly investigated bulk materials in macro-electrochemical cells. Therefore, in order to comprehend the fundamental doping-induced charge transfer processes in graphene, the µ-droplet electrochemical technique was selected to investigate the electrostatic and electrochemical behavior of the material in an aqueous medium at a selected area (10-20 $\mu m^2$) of the material.

In brief, the monolayer of graphene prepared by the mechanical cleavage of graphite was almost defect-free and various levels of defects were then induced in the exfoliated graphene by oxygen plasma treatment. The graphene was contacted by a silver paste and served as a working electrode (WE) in the experiments. In addition, CVD graphene with defects induced during preparation (on Cu foil) or transfer on $Si/SiO_2$ (~300 nm) substrate was used for comparison. A micro-capillary of borosilicate glass prepared in-house was filled with 6 M LiCl aqueous electrolyte solution and an encapsulated Pt and chlorinated silver wire were used as counter (CE) and reference electrodes (RE), respectively. A micro-manipulator device connected to a pico-pump was used to control the shape, volume and diameter of the droplet under a continuous flow of Ar gas. The electrochemical measurements were performed by using the potentiostat (Autolab, Metrohm) and the changes in crystal and electronic structure were monitored real-time by Raman spectroscopy. The photo and schematic diagram of the experimental setup are shown in Figure 8.

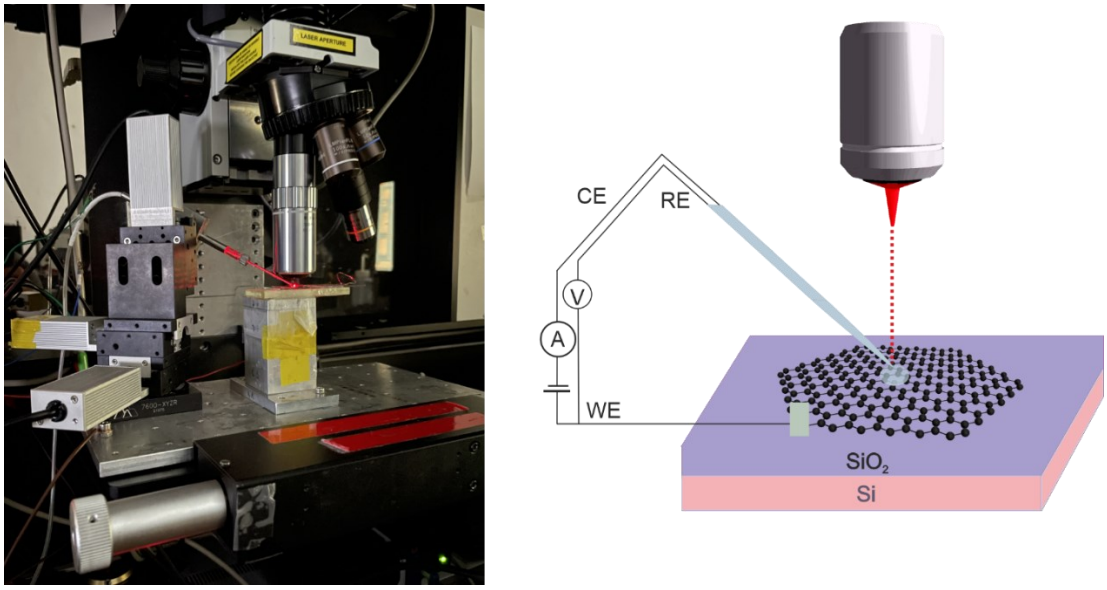


**Figure 8**: Right, photograph of the μ-droplet Raman SEC experimental setup. Left, schematic illustration of the μ-droplet SEC setup.

### 3.1.1 Charge transfer process through defect-free and defect-rich basal plane of graphene

The *in-situ* μ-droplet SEC setup, shown in Figure 8, was used to distinguish between localized charge transfer processes through the pristine and defective regions of the graphene basal plane. As shown in Appendix 1, the doping-induced charge transfer process in defect-free and defective graphene exhibits distinct behavior in Raman spectra. The inter-defect density ($L_D$) was estimated by using the $I_D/I_G$ from Raman spectra as was reported by Cancado *et al.,*[48]. The calculated $L_D$ is mentioned in Table S1, Appendix 2.

$$L_D^2\ (nm^2) = (1.8 \pm 0.5) \times 10^{-19} \lambda_L^4 \left(\frac{I_D}{I_G}\right)^{-1} \quad (1)$$

The influence of the defects on charge transfer doping is an important aspect that has not been explored properly. However, so far, various *in-situ* Raman experiments have been conducted by

covering the entire graphene sheet with electrolyte [55,88,89]. Such standard experiments do not provide information about the role of defects in doping-induced changes in a specific area. In order to understand such doping (defect, in this case) dependent charge transfer in localized monolayer graphene, *in-situ* Raman SEC measurements were performed in a potential range of 0 to 1.4 V for mechanically exfoliated graphene and from 0 to 1.2 V for CVD graphene using 6 M LiCl aqueous electrolyte. In Figure 1, appendix 1, Raman spectra, measured at 0 V on pristine exfoliated monolayer graphene, CVD graphene, and exfoliated graphene with oxygen plasma-induced defects are shown. The D band intensity confirms that the exfoliated graphene is defect free while CVD graphene has a moderate defect content. The pristine exfoliated graphene was exposed to oxygen plasma of two different exposure times in two separate samples which resulted in the average $L_D$ values of 72 and 24 nm. Those samples are named as $L_{D\text{-}72}$ and $L_{D\text{-}24}$, respectively.

In Figure 2, appendix 1, the G peak, being the most sensitive to the external perturbation, was blue shifted with the application of potential from 0 to 1.4 V (for pristine exfoliated graphene) which is attributed to the hole doping. Importantly, the splitting of G peak into two sub-bands (referred to as $G_I$ and $G_D$) at 1 V originated from signals stemming from intact and defective graphene regions as shown in Figure 9. Both sub-bands continued to blue shift with the increase of hole concentration. The shift rate of Raman frequency *per* applied potential ($\Delta\omega/\Delta V$) of the non-splitted G band at potential range of 0.2 V— 0.8 V were observed to be 13.9 $cm^{-1}$/V and 20.9 $cm^{-1}$/V for pristine exfoliated graphene and CVD graphene, respectively. In the same potential range, $\Delta\omega/\Delta V$ of 16.7 $cm^{-1}$/V and 24.0 $cm^{-1}$/V were recorded for $L_{D\text{-}72}$ and $L_{D\text{-}24}$, respectively. After the G band splitting, $\Delta\omega/\Delta V$ of 18.4 $cm^{-1}$/V and 20.1 $cm^{-1}$/V for $G_D$ band in pristine exfoliated graphene and CVD graphene, respectively, were observed in the range of 0.8 V−1.2 V. Importantly, the $G_D$ band shift of pristine exfoliated graphene falls within the range of shift of the unsplit G peak of CVD

graphene. It was noticed that the initial shift rate and the potential, at which the splitting of the G band appears, were increasing with the increase in defect density.

The deep understanding of the root cause of the splitting of the G band was the main objective of this study. It was clearly shown that the shift rates were in the order of $L_{D\text{-}24} > L_{D\text{-}72} >$ pristine exfoliated graphene. The splitting of the G peak in pristine graphene took place at higher potential, but there was no splitting in the CVD graphene. We summarized from the observation of the G peak that the charge transfer proceeded through the existing defects in CVD graphene and the contribution from the basal plane was negligible. Due to the (near) absence of defects in pristine exfoliated graphene and the μ-droplet placement inside the flake, there was scarce possibility for the charge carriers to enter the graphene through the defects or flake edges. Initially, the charge transfer proceeded at a slower rate through the basal plane, resulting to a lower G peak shift rate. At higher potentials, defects were probably created which favored the charge transfer *via* defects and resulted in a higher G peak shift. However, large portions of the surface were still defect-free, which results in a bimodal – slow and fast – distribution of charge transfer processes. The hole concentration was calculated to be about $1.0 \times 10^{13}$ and $2.4 \times 10^{13}$ $cm^{-2}$ [55] for the defect-free and defect-rich regions, respectively, for pristine exfoliated graphene at 1.3V. For exfoliated graphene with plasma-induced defects, faster charge transfer was visible at lower potentials while the bimodal process distribution was manifested at higher potentials.

Furthermore, by using cyclic voltammetry with hexaammineruthenium complex $[Ru\text{-}(NH_3)_6]^{3+/2+}$ to evaluate the electron transfer activity of different graphene samples, the idea of the two charge transfer processes with different rates was supported. The heterogeneous electron transfer rate constant ($k^0$) was calculated from the cyclic voltammograms at scan rates varying from 0.75 to 3.5

$Vs^{-1}$. The lower value of $k^0$ for pristine exfoliated graphene in comparison to CVD graphene demonstrate the slower kinetics at the almost perfect basal plane. The oxygen plasma-treated exfoliated graphene samples $L_{D\text{-}24}$ and $L_{D\text{-}72}$ showed two different values of $k^0$ that corresponded to two different charge transfer processes as reported in appendix 1. The two different charge transfer processes through basal plane and defect-rich regions are shown schematically in Figure 9.

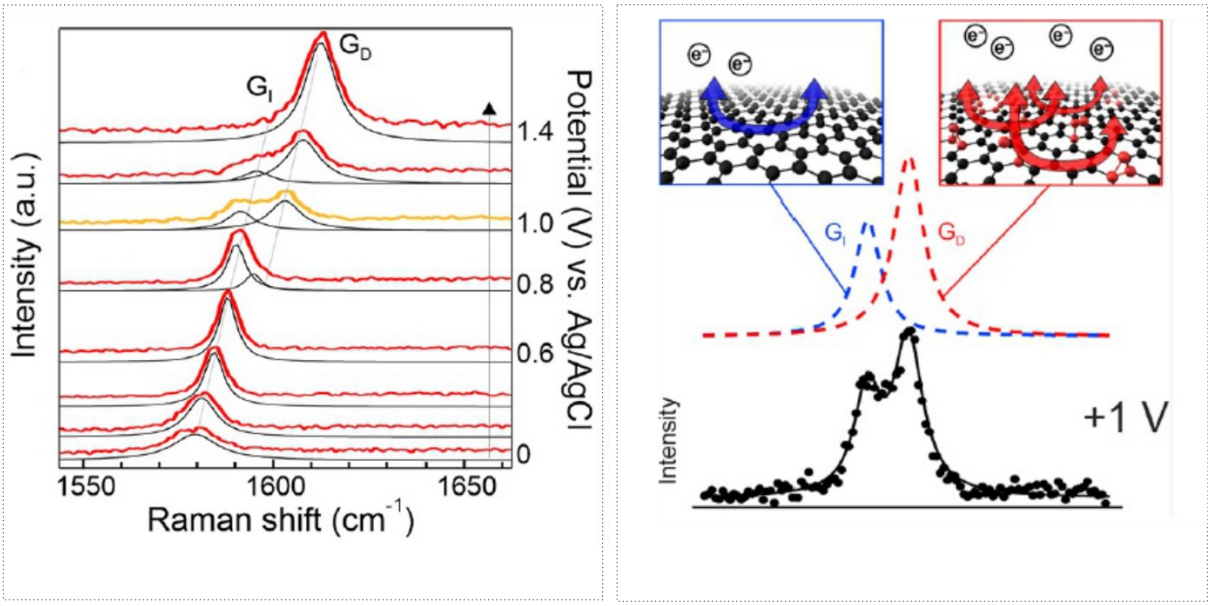


**Figure 9**: Left, the evolution of $G_I$ and $G_D$ peaks in Raman spectra of graphene corresponding to two different charge transfer processes in defect-free and defective graphene. Right, schematic illustration of the charge transfer processes in defect-free and defect-rich graphene [57].

## 3.2 Monitoring the reversible (de)intercalation of anion into graphite by *in-situ* Raman SEC in concentrated aqueous electrolyte solution

### 3.2.1 The influence of structural properties on the electrochemical (de)intercalation of $ClO_4^-$ anion into graphite

The electrochemical properties and structural parameters of natural graphite (NG) and kish graphite (KG) were compared in this study. The structural parameters such as degree of graphitization ($g$) and coherent domain size along the $c$-axis ($L_c$) for NG and KG were determined from XRD (Figure 1, appendix 2) based on the precise determination of $2\theta$, interlayer spacing ($d_{002}$), and full width at half maxima (FWHM) ($\beta$) of the 002 reflection. The degree of graphitization can be calculated by using the following equation [90].

$$g\ (\%) = \frac{0.3440 - d_{002}}{0.3440 - 0.3354} \times 100 \quad (2)$$

where 0.3440 is the interlayer spacing of non-graphitized carbon and 0.3354 is the interlayer spacing of ideal graphite crystal. The interlayer spacing $d_{002}$ quantified from XRD of graphite, were used to calculate the degree of graphitization.

The coherent domain size ($L_c$) can be calculated by using the Scherrer equation as follows [91,92]:

$$L_c = \frac{k\lambda}{\beta cos\Theta} \quad (3)$$

where $k$ is the Scherrer constant and has a value of 0.89 for in the $c$-axis direction, $\lambda$ is the wavelength of the incident X-rays, $\beta$ (radian) is the FWHM of the respective XRD peak, and $\theta$ is the observed Bragg's angle.

Raman spectroscopy has been widely used to probe the disorder in the crystal lattice of graphite. Eventually, defects are of great importance due to modulation in the electronic properties of the graphite [45,93]. In Figure 1, appendix 2, the ratio of the disorder-induced D peak to the G peak ($I_D/I_G$) of NG and KG was used to calculate the lateral domain size along the *a*-axis ($L_a$) of crystallite by the following equation [47];

$$L_a(nm) = 2.4 \times 10^{-10} \lambda_L^4 \left(\frac{I_D}{I_G}\right)^{-1} \quad (4)$$

where $\lambda_L$ is the wavelength of the laser used to excite the Raman scattering.

The $I_D/I_G$ ratio can also be used to calculate the defect density ($n_D$) by the following equation [48]. The calculated parameters are given in Table 1 in appendix 2.

$$n_D\ (cm^{-2}) = \frac{(1.8 \pm 0.5) \times 10^{22}}{\lambda_L^4} \left(\frac{I_D}{I_G}\right) \quad (5)$$

Prior to the electrochemical measurements for the preparation of electrodes, a slurry consisting of commercial NG (Nacional de Grafite, Ltda) or KG (Graphene Supermarket) powder, conducting carbon black, polyvinylidene difluoride (PVDF) binder (75:15:10 wt. ratio), and N-methyl-2-pyrrolidone (NMP) was casted on a current collector made of polytetrafluoroethylene (PTFE)-treated hydrophobic carbon paper (150–200 μm thick; 120 Toray Carbon paper, Fuel Cell Store, USA). The as-prepared electrodes were dried at 80 °C under a vacuum in an oven for 12 h, Electrochemical measurements were carried out in 2.4 M $Al(ClO_4)_3$ aqueous electrolyte solution in three electrode systems: NG/KG as the working electrode, Pt as the counter electrode and Ag/AgCl as the pseudo-reference electrode. The electrochemical measurements were performed using a μ-Autolab type III workstation. The cyclic voltammetry (CV) tests were conducted in the

potential window of −0.08 to 1.58 V (*vs.* Ag/AgCl). The (de)intercalation of an anion into graphite was attributed to two sets of redox peaks in CV recorded at a sweep rate of 5 $mVs^{-1}$ as shown in Figure 2 of appendix 2. The sets of the redox peaks in CV were in line with the galvanostatic charge/discharge potential profiles of the NG and the KG recorded at a current density of 250 $mAg^{-1}$ shown in Figure 2 in appendix 2.

Furthermore, in order to investigate the intercalation of the $ClO_4^-$ anion into graphite, various *ex-situ* characterizations such as XRD, Raman spectroscopy, FTIR-ATR and XPS of pristine, charged, and discharged graphite were performed. The XRD $d_{002}$ reflection at $2\theta$ of 26.5° split into two peaks at 26.6° and 26.9° in the charged state which demonstrated the intercalation of the $ClO_4^-$ anion into the interlayer space as shown in Figure 3, appendix 2. The *ex-situ* Raman spectra of the charged NG with increased $I_D/I_G$ (0.73) in comparison to the discharged (0.53) and pristine (0.43) state provided a solid evidence for the intercalation of the $ClO_4^-$ anion. Similarly, *ex-situ* Raman spectra of the charged KG revealed the increase of $I_D/I_G$ (0.41) in comparison to the discharged (0.20) and pristine (0.05) states as documented in Figure 4 in appendix 2.

The *in-situ* Raman SEC has been demonstrated to be a versatile tool for studying carbon materials ranging from a few-layer graphene to bulk graphite in order to gain deeper insights into ionic intercalation [82,83,94]. We performed *in-situ* Raman SEC of the NG and KG in "bulk" electrolyte by using the home-made macro spectroelectrochemical cell. A schematic representation of the cell used for *in-situ* Raman SEC is shown in Figure 10.

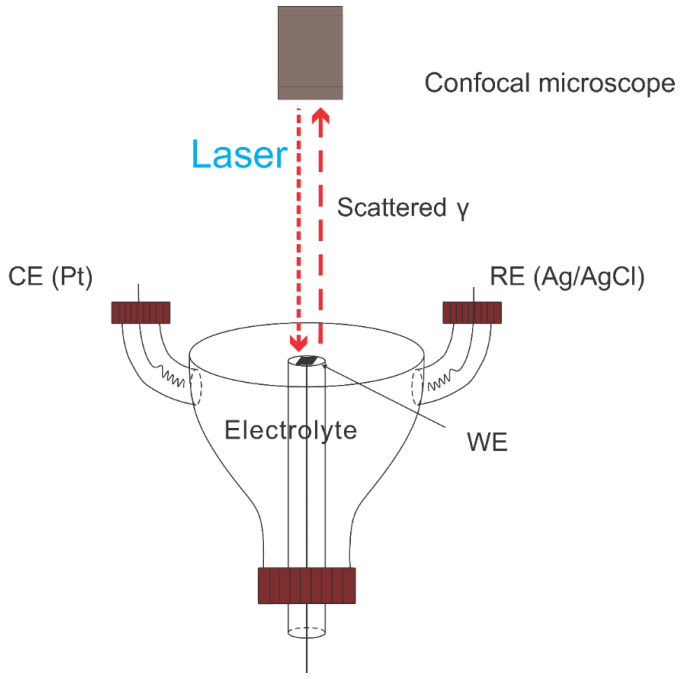


**Figure 10:** Schematic illustration of the cell used for *in-situ* Raman SEC studies of graphite at macroscale. CE, RE, and WE stand for counter, reference and working electrode, respectively.

The Raman G band of graphitic carbons is known to be sensitive to the interaction of ionic species in the interlayer galleries and the formation of GICs [95–97]. During the charging half cycle, at approximately 1.45V (against Ag/AgCl), the G peak was splitted into two components (Figure 11). The low-frequency (~1584 $cm^{-1}$) $E_{2g}$(i) mode originates from the vibration of the $sp^2$ carbon atoms of the non-intercalated (interior) graphite layers, and the high-frequency (~1616 $cm^{-1}$) $E_{2g}$(b) mode corresponds to the vibration of the carbon atoms from the boundary layers that accommodate the intercalated $ClO_4^-$ ions. Upon a further increase in the potential, the intensity of the $E_{2g}$(b) peak increased due to the gradual rise of the $ClO_4^-$ ion concentration in the graphite interlayer spaces [94]. The *in-situ* Raman SEC of KG represented a similar behavior like NG but the (de)intercalation process was less reversible in this case (Figure 11 right).

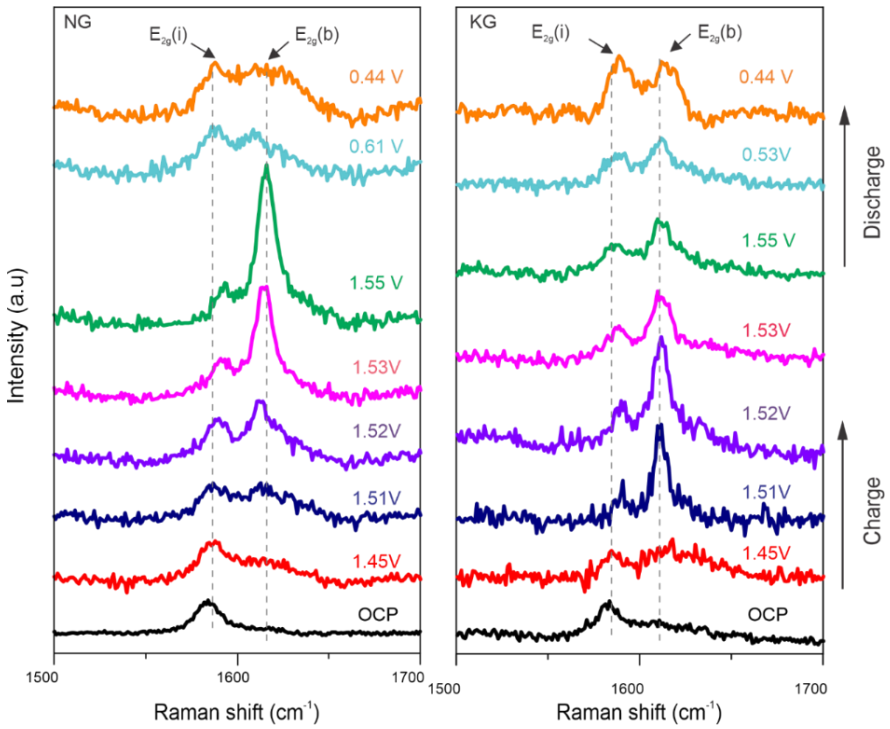


**Figure 11**: *In-situ* Raman SEC of (left) NG and (right) KG during the charge/discharge process in 2.4M $Al(ClO_4)_3$ aqueous electrolyte solution.

Analysis of CVs at different sweep rates was performed to explore whether the $ClO_4^-$ anion (de)intercalation process was diffusion or surface-controlled or both. This can be found out by examining the relationship between peak currents ($i$) and scan rate ($v$) determined from CV. The power-law relationship can be written as [98,99]:

$$i = a\, v^b \tag{6}$$

where $a$ and $b$ are adjustable parameters. The $b$ value can be obtained from the slope of the *log(i) vs. log(v)* plot. The value of $b = 0.5$ indicates that the charge/discharge process is controlled by ion diffusion, while $b = 1$ indicates a purely surface-controlled process. The $b$ value between 0.5 and 1.0 corresponds to the presence of both surface and diffusion-controlled processes. The

relative contributions of charge storage with respect to the surface and diffusion-controlled processes were calculated from the deconvoluted currents of CV for various scan rates (1 to 7 $mVs^{-1}$) for the NG and the KG. The following relation was used to calculate the contribution of the individual processes [98,100].

$$i = k_1 v + k_2 v^{1/2} \quad (7)$$

where $k_1 v$ represents the surface-controlled process, and $k_2 v^{1/2}$ is the ionic diffusion [98,99].

The reversible (de)intercalation in the NG resulted in a stable electrochemical performance: discharge capacity of ~20 $mAhg^{-1}$ at a current density of 250 $mAg^{-1}$ with high Coulombic efficiency (> 80%) that could be attributed to its small crystallite size, $L_a$. On the one hand, we observed a higher discharge capacity of ~30 $mAhg^{-1}$ at a current density of 250 $mAg^{-1}$ for the KG (Figure 7, appendix 2) which can be attributed to the higher structural order and the lower defect content. On the other hand, the electrochemical (de)intercalation of $ClO_4^-$ was more irreversible in comparison to NG because of the larger crystallite domain size of KG compared to NG, making it difficult for the large size $ClO_4^-$ anions to (de)intercalate from KG.

### 3.2.2 The effect of ultrasound treatment of graphite on the reversibility of anion (de)intercalation

In this study, we investigated the effects of mild ultrasound treatment of graphite on the reversibility of $ClO_4^-$ anion (de)intercalation in a 2.4 M $Al(ClO_4)_3$ aqueous solution. The ultrasound treatment of natural graphite (NG) induced the formation defects in the crystal lattice

of the ultrasonicated graphite (US-NG) and reduced its lateral domain size, $L_a$. The smaller $L_a$ enhanced the reversibility of (de)intercalation of the $ClO_4^-$ anion. The structural parameters, degree of graphitization ($g$) and coherent domain size along $c$-axis ($L_c$), for US-NG were quantified from XRD and the inter-defect distance ($L_D$), defect density ($n_D$), and $L_a$ were calculated from the $I_D/I_G$ Raman intensity ratio (Figure 1, appendix 3) by using the equations 2 to 5. The calculated parameters for all the samples are presented in Table 1, appendix 3.

The two sets of redox peaks in CV illustrated the electrochemical (de)intercalation of the $ClO_4^-$ ions in the graphite as was shown in Figure 2, appendix 3. The difference in galvanostatic charge/discharge profile for US-NG and NG at 250 $mAg^{-1}$ was attributed to the influence of structural parameters on the electrochemical properties of the samples. Stable electrochemical performance with discharge capacity of ~18 $mAhg^{-1}$ over 300 cycles at a current density of 250 $mAg^{-1}$ was observed in US-NG. The reversible (de)intercalation of $ClO_4^-$ anion in US-NG provides the longer cyclic stability that could be due to its small crystallite size.

The reversible (de)intercalation of $ClO_4^-$ anion into US-NG during the discharge process was monitored by *in-situ* Raman SEC using the home-made cell in a three-electrode setup as was shown in Figure 10. During the charging process, the G peak at 1.40 V (vs. Ag/AgCl) splits into $E_{2g}$ (i) and $E_{2g}$(b) modes, with the intensity of the $E_{2g}$(b) peak increasing further, corresponding to the gradual intercalation of $ClO_4^-$ ions into graphite interlayer spaces. The complete disappearance of the $E_{2g}$(b) mode during the discharge process is attributed to the reversible (de)intercalation of the anion [83]. The *in-situ* Raman SEC thus revealed the reversible (de)intercalation of $ClO_4^-$ anion into US-NG which is shown in Figure 12.

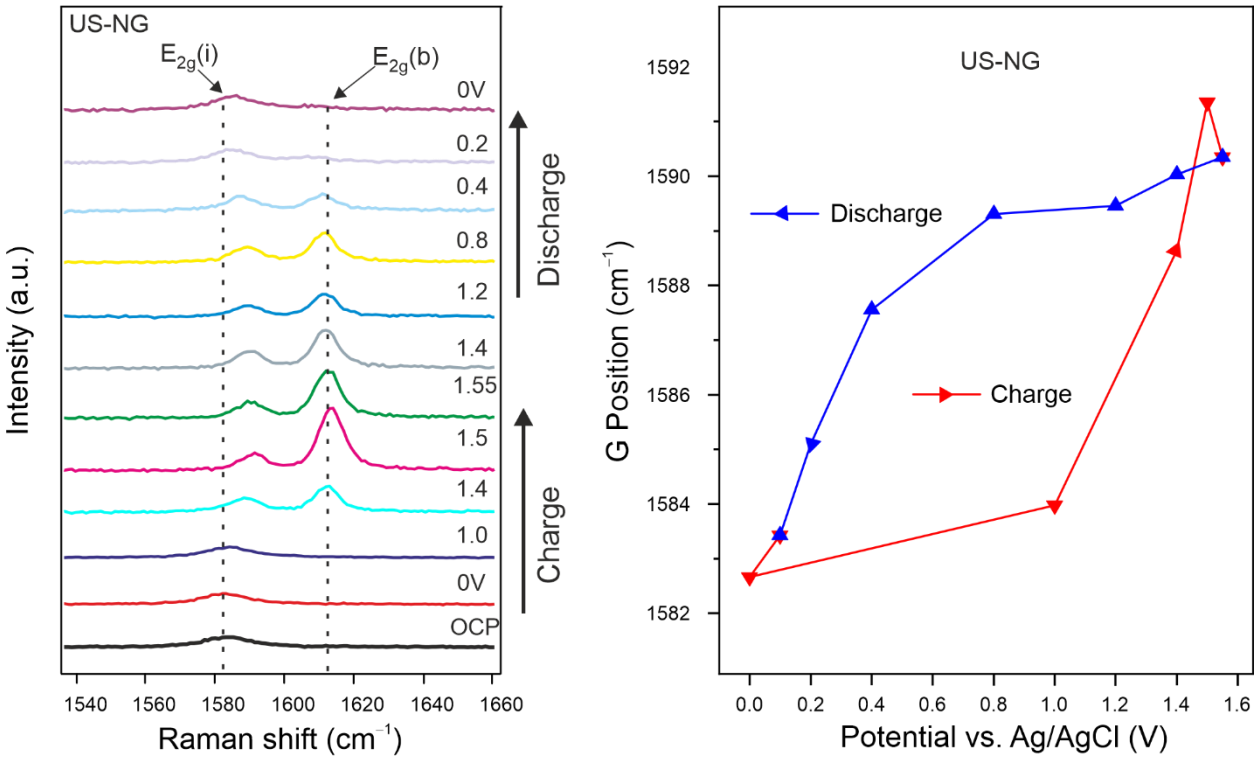


**Figure 12**: *In-situ* Raman spectroelectrochemistry of US-NG during charge/discharge process in 2.4 M $Al(ClO_4)_3$ aqueous electrolyte: left, Evolution of the Raman spectra in the G peak spectral region; right, Raman G peak ($E_{2g}$ (i)) position evolution fitted as one Lorentzian line shape. The applied potentials were held for 1000 s for each step.

Furthermore, in order to get deeper insights and to explore the changes in lattice structure upon the formation of GICs during charge/discharge process, *operando* XRD has been proved to be a promising technique for batteries research [101,102]. O*perando* analysis of US-NG during charge/discharge was performed by XRD where X-rays penetrated through the electrode window from the top, sealed by the KAPTON tape. The characteristic graphitic 002 reflection shifted toward lower and higher $2\theta$ ($00n$+1 and $00n$+2 reflections) during the charge process, which was attributed to the intercalation of the anion into graphite [103]. The splitting of the 004 reflection into two prominent peaks during the charge process also manifested the intercalation of the $ClO_4^-$ anion into graphite. The *operando* XRD analysis of US-NG during the charge/discharge process

in 2.4 M $Al(ClO_4)_3$ aq. electrolyte solution is presented in Figure 13. To describe the intercalation process in more detail, further *ex-situ* spectroscopic techniques, such as Raman spectroscopy and XPS on the fresh, charged, and discharged electrodes were performed. The *ex-situ* XPS helped in obtaining a quantitative view on the $ClO_4^-$ anion intercalation as presented in Figure 5, appendix 3.

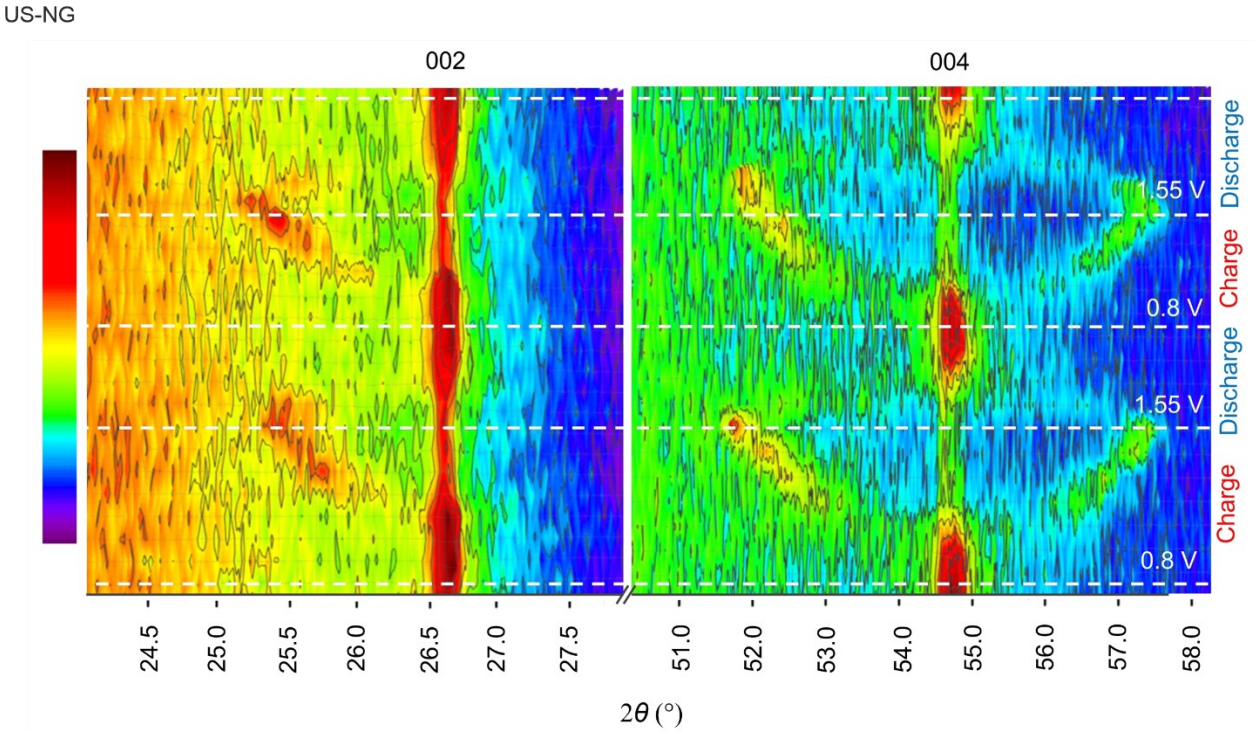


**Figure 13**: *Operando* XRD analysis of US-NG during charge and discharge using 2.4 M $Al(ClO_4)_3$ aq. electrolyte solution.

### 3.2.3 Anion intercalation into graphite from aluminum perchlorate based "water in salt" electrolyte

In this study, we reported the intercalation/deintercalation of an anion into graphite using a 15 m "water in salt" (WISE) electrolyte of aluminum perchlorate. We achieved a highly stable electrochemical window of 4.0 V that offered a reversible (de)intercalation of $ClO_4^-$ anion into graphite (Figure 2, appendix, 4). The WISE electrolyte provided a stable galvanostatic charge/discharge cycling and high Coulombic efficiency. The galvanostatic charge/discharge cyclic stability over 2000 cycles supported the reversible (de)intercalation of $ClO_4^-$ anion in highly oriented pyrolytic graphite (HOPG) as shown in Figure 3, appendix 4.

*In-situ* Raman SEC was used to investigate the (de)intercalation of the $ClO_4^-$ anion. The G peak was splitted into two components during the charging half cycle: the low-frequency (1574 $cm^{-1}$) $E_{2g}$(i) mode and the high-frequency (1612 $cm^{-1}$) $E_{2g}$(b) mode, as was also observed in sections 3.2.1 and 3.2.2; the latter mode corresponds to the vibration of the carbon atoms in graphite layers that accommodate the intercalated $ClO_4^-$ anion. The $E_{2g}$(b) peak was reversed to its original position, demonstrating the reversibility of anion (de)intercalation during the discharge process [78]. The *ex-situ* XPS analysis was also performed to demonstrate the (de)intercalation of $ClO_4^-$ anion in graphite. The higher peak intensity in the charged graphite in comparison to the discharged one illustrated the (de)intercalation of the $ClO_4^-$ anion (Figure 4, appendix 4). Additionally, *operando* XRD analysis was used to investigate the changes in the graphite structure caused by the anion intercalation/deintercalation during charge/discharge (Figure 5, appendix 4). The shift of the 002 peak into lower and higher $2\theta$ reveals the anion intercalation and deintercalation during the charge and discharge process, respectively [104]. The further splitting of the 004 reflection

into two dominant peaks was also observed during the charge process which illustrates the intercalation of $ClO_4^-$ ions.

The interpretation of the staging mechanism during the charge/discharge process was also done during this study. The interlayer gallery expansion of 3.76 Å to ~7.08 Å upon charging also evidenced the intercalation of anion into graphitic galleries. The mixture of stage 4-5 was observed from the change in interlayer spacing due to intercalation of anions as shown in Figure 14.

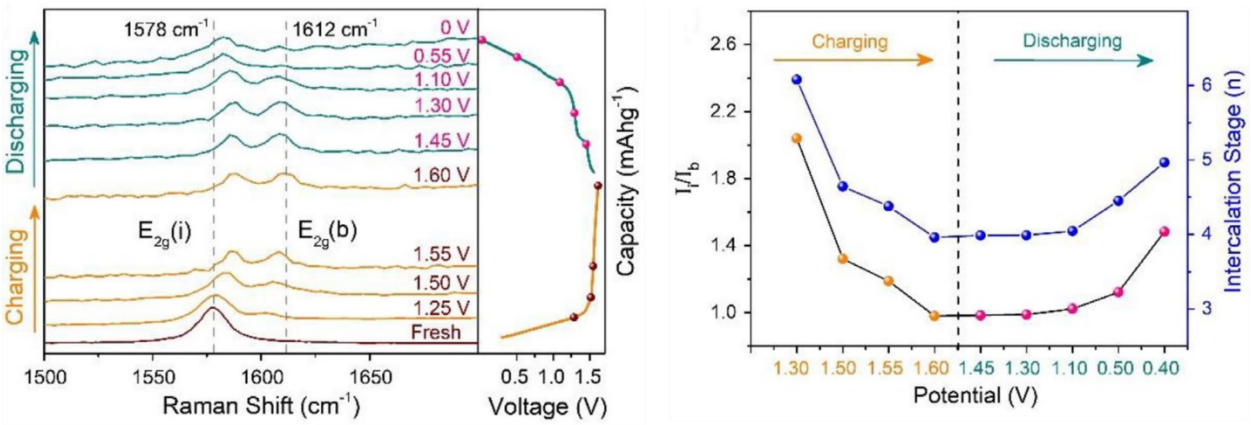


**Figure 14**: *In-situ* Raman SEC of HOPG in water-in-salt $Al(ClO_4)_3$ aqueous electrolyte: left, evolution of the Raman spectra in the G peak region during the charge/discharge process; left, the interpretation of the staging number from $I_D/I_G$ change during the charge/discharge process [74].

# 4 Conclusions

**In the 1st study – section 3.1 –** we introduced a novel μ-droplet Raman SEC method, which allows for a simultaneous electrochemical and Raman spectroscopy investigation at the micrometer lateral scale. We observed the different behavior of the two surface types in graphene in Raman spectral response by an apparent G mode splitting with the applied potential, as well as in the cyclic voltammograms using an outer-sphere redox mediator. Both observations point to different charge transfer processes with varying rates, which take place in the defect-free and defect-rich regions at the surface. Our results highlight the necessity of using localized methods when assessing the (spectro)electrochemical properties of materials with a distinctly heterogeneous surface morphology.

**The 2nd study – section 3.2.1 –** describes the reversible electrochemical (de)intercalation of $ClO_4^-$ anions in graphite (NG and KG) using a concentrated $Al(ClO_4)_3$ aqueous electrolyte and its correlation with graphite's structural properties. The higher defect content in pristine NG leads to smaller crystallite domain size ($L_a$) and higher defect density (*i.e.,* $n_D$), in comparison to pristine KG. The smaller crystallite size facilitates the release of large $ClO_4^-$ anions from the graphitic layers during the discharge process, resulting in a reversible and stable electrochemical performance of NG, compared to KG. Furthermore, extensive *ex-situ* characterizations such as XRD, Raman spectroscopy, and FTIR-ATR, and *in-situ* SEC measurements were performed to reveal the ionic (de)intercalation into graphite. The detailed discussion of anion intercalation in NG and KG, as well as the differences in their structural properties and electrochemical behavior, pave the way for smartly designed layered intercalation compounds and their applications in a

variety of fields, including environmentally friendly, non-flammable, and low-cost aqueous energy storage systems.

**In the 3rd study – section 3.2.2 –** the effect of ultrasound treatment of NG on the electrochemical (de)intercalation of the $ClO_4^-$ anion was investigated in a concentrated aqueous $Al(ClO_4)_3$ electrolyte. The ultrasonication of NG in NMP induced the formation of defects accompanied by a reduction in its $L_a$. The smaller $L_a$ of US-NG in comparison to pristine NG facilitated the easier escape of the large anions from the graphite interlayer galleries, thereby enhancing the reversibility and cyclic stability. *In-situ* Raman SEC and *operando* XRD of US-NG confirmed the reversibility of the structural changes in the graphite induced by the $ClO_4^-$ intercalation. The effect of ultrasound treatment on structural properties of graphite and its correlation with the reversibility of electrochemical intercalation processes into graphite can be helpful in designing the novel functional materials for energy storage systems.

**In the 4th study – section 3.2.3 –** the electrochemical (de)intercalation of anion into HOPG using a highly concentrated "water in salt" electrolyte of aluminum perchlorate was studied. We achieved a high stability of electrochemical window of 4.0 V which offered the reversible (de)intercalation of $ClO_4^-$ anion into graphite. The (de)intercalation processes were investigated using *ex-situ* XPS, *in-situ* Raman SEC, and *operando* XRD studies. The WISE electrolyte provides the stable galvanostatic charge/discharge performance for 2000 cycles and high Coulombic efficiency of over 95%.

# 5 References


[1] B.J. Kim, S.K. Lee, M.S. Kang, J.H. Ahn, J.H. Cho, Coplanar-gate transparent graphene transistors and inverters on plastic, ACS Nano 6 (2012) 8646–8651.

[2] A.C. Ferrari, D.M. Basko, Raman spectroscopy as a versatile tool for studying the properties of graphene, Nat. Nanotechnol. 8 (2013) 235–246.

[3] M.J. Allen, V.C. Tung, R.B. Kaner, Honeycomb carbon: A review of graphene, Chem. Rev. 110 (2010) 132–145.

[4] E. Ji, M.J. Kim, J.Y. Lee, D. Sung, N. Kim, J.W. Park, S. Hong, G.H. Lee, Substrate effect on doping and degradation of graphene, Carbon 184 (2021) 651–658.

[5] G. Yang, L. Li, W.B. Lee, M.C. Ng, Structure of graphene and its disorders: a review, Sci. Technol. Adv. Mater. 19 (2018) 613–648.

[6] A.C. Neto, F. Guinea, N.M. Peres, Drawing conclusions from graphene, Phys. World 19 (2006) 33–37.

[7] L.M. Malard, M.A. Pimenta, G. Dresselhaus, M.S. Dresselhaus, Raman spectroscopy in graphene, Phys. Rep. 473 (2009) 51–87.

[8] Y. Yang, Y.C. Zou, C.R. Woods, Y. Shi, J. Yin, S. Xu, S. Ozdemir, T. Taniguchi, K. Watanabe, A.K. Geim, K.S. Novoselov, S.J. Haigh, A. Mishchenko, Stacking Order in Graphite Films Controlled by van der Waals Technology, Nano Lett. 19 (2019) 8526–8532.

[9] K. S. Novoselov, A. K. Geim, S. V. Morozov, D. Jiang, Y. Zhang, S. V. Dubonos, I. V. Grigorieva, A. A. Firsov, Electric Field Effect in Atomically Thin Carbon Films, Science 306 (2004) 666–669.

[10] M. Yi, Z. Shen, A review on mechanical exfoliation for the scalable production of graphene, J. Mater. Chem. A 3 (2015) 11700–11715.

[11] Y. Hernandez, V. Nicolosi, M. Lotya, F.M. Blighe, Z. Sun, S. De, B. Holland, M. Byrne, Y. Gun, J. Boland, P. Niraj, G. Duesberg, S. Krishnamurthy, R. Goodhue, J. Hutchison, V.

Scardaci, A.C. Ferrari, J.N. Coleman, Nat. Nanotechnol. 3 (2008) 563–568.

[12] O. Frank, M. Kalbac, Chemical vapor deposition (CVD) growth of graphene films, Graphene Prop. Prep. Characterisation Devices, Graphene, Woodhead Publishing (2014) 27–49.

[13] B. Huet, J.P. Raskin, Pressure-Controlled Chemical Vapor Deposition of Single-Layer Graphene with Millimeter-Size Domains on Thin Copper Film, Chem. Mater. 29 (2017) 3431–3440.

[14] R. Fates, H. Bouridah, J.P. Raskin, Probing carrier concentration in gated single, bi- and tri-layer CVD graphene using Raman spectroscopy, Carbon 149 (2019) 390–399.

[15] M. Chen, G. Li, W. Li, D. Stekovic, B. Arkook, M.E. Itkis, A. Pekker, E. Bekyarova, R.C. Haddon, Large-scale cellulose-assisted transfer of graphene toward industrial applications, Carbon 110 (2016) 286–291.

[16] K.F. Mak, L. Ju, F. Wang, T.F. Heinz, Optical spectroscopy of graphene: From the far infrared to the ultraviolet, Solid State Commun. 152 (2012) 1341–1349.

[17] A.H. Castro Neto, F. Guinea, N.M.R. Peres, K.S. Novoselov, A.K. Geim, The electronic properties of graphene, Rev. Mod. Phys. 81 (2009) 109–162.

[18] K.F. Mak, J. Shan, T.F. Heinz, Electronic structure of few-layer graphene: Experimental demonstration of strong dependence on stacking sequence, Phys. Rev. Lett. 104 (2010) 1–4.

[19] Y. Zhang, Y.W. Tan, H.L. Stormer, P. Kim, Experimental observation of the quantum Hall effect and Berry's phase in graphene, Nature 438 (2005) 201–204.

[20] K.S. Novoselov, A.K. Geim, S. V. Morozov, D. Jiang, M.I. Katsnelson, I. V. Grigorieva, S. V. Dubonos, A.A. Firsov, Two-dimensional gas of massless Dirac fermions in graphene, Nature 438 (2005) 197–200.

[21] S. Fujii, T. Enoki, Structure and Nanofabrication, Acc. Chem. Res. 46 (2012) 2202–2210.

[22] H. Xu, L. Xie, H. Zhang, J. Zhang, Effect of graphene Fermi level on the Raman scattering intensity of molecules on graphene, ACS Nano 5 (2011) 5338–5344.

[23] A.C. Ferrari, Raman spectroscopy of graphene and graphite: Disorder, electron-phonon coupling, doping and nonadiabatic effects, Solid State Commun. 143 (2007) 47–57.

[24] R. Beams, L. Gustavo Cançado, L. Novotny, Raman characterization of defects and dopants in graphene, J. Phys. Condens. Matter 27 (2015) 083002.

[25] J.H. Zhong, J.Y. Liu, Q. Li, M.G. Li, Z.C. Zeng, S. Hu, D.Y. Wu, W. Cai, B. Ren, Interfacial capacitance of graphene: Correlated differential capacitance and in situ electrochemical Raman spectroscopy study, Electrochim. Acta 110 (2013) 754–761.

[26] J. Binder, J.M. Urban, R. Stepniewski, W. Strupinski, A. Wysmolek, In situ Raman spectroscopy of the graphene/water interface of a solution-gated field-effect transistor: Electron-phonon coupling and spectroelectrochemistry, Nanotechnology 27 (2015) 045704.

[27] A. Das, B. Chakraborty, S. Piscanec, S. Pisana, A.K. Sood, A.C. Ferrari, Phonon renormalization in doped bilayer graphene, Phys. Rev. B - Condens. Matter Mater. Phys. 79 (2009) 1–7.

[28] M.A. Pimenta, G. Dresselhaus, M.S. Dresselhaus, L.G. Cançado, A. Jorio, R. Saito, Studying disorder in graphite-based systems by Raman spectroscopy, Phys. Chem. Chem. Phys. 9 (2007) 1276–1291.

[29] M. Dieng, M. Bensifia, J. Borme, I. Florea, C.M. Abreu, C. Jama, C. Léonard, P. Alpuim, D. Pribat, A. Yassar, F.Z. Bouanis, Wet-Chemical Noncovalent Functionalization of CVD Graphene: Molecular Doping and Its Effect on Electrolyte-Gated Graphene Field-Effect Transistor Characteristics, J. Phys. Chem. C. 126 (2022) 4522–4533.

[30] M. Lazzeri, C. Attaccalite, L. Wirtz, F. Mauri, Impact of the electron-electron correlation on phonon dispersion: Failure of LDA and GGA DFT functionals in graphene and graphite, Phys. Rev. B - Condens. Matter Mater. Phys. 78 (2008) 8–11.

[31] M.S. Dresselhaus, A. Jorio, R. Saito, Characterizing graphene, graphite, and carbon

nanotubes by Raman spectroscopy, Annu. Rev. Condens. Matter Phys. 1 (2010) 89–108.

[32] M.M. Lucchese, F. Stavale, E.H.M. Ferreira, C. Vilani, M.V.O. Moutinho, R.B. Capaz, C.A. Achete, A. Jorio, Quantifying ion-induced defects and Raman relaxation length in graphene, Carbon 48 (2010) 1592–1597.

[33] I. Childres, L.A. Jauregui, W. Park, H. Caoa, Y.P. Chena, Raman spectroscopy of graphene and related materials, New Dev. Phot. Mater. Res. 1 (2013) 403–418.

[34] A.C. Ferrari, J. Robertson, Raman spectroscopy of amorphous, nanostructured, diamond-like carbon, and nanodiamond, Philos. Trans. R. Soc. A Math. Phys. Eng. Sci. 362 (2004) 2477–2512.

[35] A.M. Rao, E. Richter, S. Bandow, B. Chase, P.C. Eklund, K.A. Williams, S. Fang, K.R. Subbaswamy, M. Menon, A. Thess, R.E. Smalley, G. Dresselhaus, M.S. Dresselhaus, Diameter-selective Raman scattering from vibrational modes in carbon nanotubes, Science 275 (1997) 187–190.

[36] M.S. Dresselhaus, G. Dresselhaus, R. Saito, A. Jorio, Raman spectroscopy of carbon nanotubes, Phys. Rep. 409 (2005) 47–99.

[37] O. Frank, M.S. Dresselhaus, M. Kalbac, Raman spectroscopy and in Situ Raman spectroelectrochemistry of isotopically engineered graphene systems, Acc. Chem. Res. 48 (2015) 111–118.

[38] M. Kalbac, H. Farhat, J. Kong, P. Janda, L. Kavan, M.S. Dresselhaus, Raman spectroscopy and in situ raman spectroelectrochemistry of bilayer 12C/13C graphene, Nano Lett. 11 (2011) 1957–1963.

[39] N.S. Mueller, S. Heeg, M.P. Alvarez, P. Kusch, S. Wasserroth, N. Clark, F. Schedin, J. Parthenios, K. Papagelis, C. Galiotis, M. Kalbáč, A. Vijayaraghavan, U. Huebner, R. Gorbachev, O. Frank, S. Reich, Evaluating arbitrary strain configurations and doping in graphene with Raman spectroscopy, 2D Mater. 5 (2018) 015016.

[40] M.A. Brown, M.S. Crosser, M.R. Leyden, Y. Qi, E.D. Minot, Measurement of high carrier

mobility in graphene in an aqueous electrolyte environment, Appl. Phys. Lett. 109 (2016) 093104.

[41] L.H. Hess, M. V. Hauf, M. Seifert, F. Speck, T. Seyller, M. Stutzmann, I.D. Sharp, J.A. Garrido, High-transconductance graphene solution-gated field effect transistors, Appl. Phys. Lett. 99 (2011) 2009–2012.

[42] S. Ryu, L. Liu, S. Berciaud, Y.J. Yu, H. Liu, P. Kim, G.W. Flynn, L.E. Brus, Atmospheric oxygen binding and hole doping in deformed graphene on a SiO2 substrate, Nano Lett. 10 (2010) 4944–4951.

[43] M. Velický, P.S. Toth, From two-dimensional materials to their heterostructures: An electrochemist's perspective, Appl. Mater. Today 8 (2017) 68–103.

[44] X. Jia, M. Hu, K. Soundarapandian, X. Yu, Z. Liu, Z. Chen, A. Narita, K. Müllen, F.H.L. Koppens, J. Jiang, K.J. Tielrooij, M. Bonn, H.I. Wang, Kinetic Ionic Permeation and Interfacial Doping of Supported Graphene, Nano Lett. 19 (2019) 9029–9036.

[45] M. Bruna, A.K. Ott, M. Ijäs, D. Yoon, U. Sassi, A.C. Ferrari, Doping dependence of the Raman spectrum of defected graphene, ACS Nano 8 (2014) 7432–7441.

[46] A. Eckmann, A. Felten, A. Mishchenko, L. Britnell, R. Krupke, K.S. Novoselov, C. Casiraghi, Probing the nature of defects in graphene by Raman spectroscopy, Nano Lett. 12 (2012) 3925–3930.

[47] L.G. Caņado, K. Takai, T. Enoki, M. Endo, Y.A. Kim, H. Mizusaki, A. Jorio, L.N. Coelho, R. Magalhães-Paniago, M.A. Pimenta, General equation for the determination of the crystallite size la of nanographite by Raman spectroscopy, Appl. Phys. Lett. 88 (2006) 1–4.

[48] L.G. Cançado, A. Jorio, E.H.M. Ferreira, F. Stavale, C.A. Achete, R.B. Capaz, M.V.O. Moutinho, A. Lombardo, T.S. Kulmala, A.C. Ferrari, Quantifying defects in graphene via Raman spectroscopy at different excitation energies, Nano Lett. 11 (2011) 3190–3196.

[49] TUINSTRA F, KOENIG JL, Raman Spectrum of Graphite, J. Chem. Phys. 53 (1970) 1126–1130.

[50] A. Cortijo, M.A.H. Vozmediano, Effects of topological defects and local curvature on the electronic properties of planar graphene, Nucl. Phys. B. 763 (2007) 293–308.

[51] T. Xu, L. Sun, Structural defects in graphene, Defects Adv. Electron. Mater. Nov. Low Dimens. Struct. 5 (2018) 137–160.

[52] V. Passi, A. Gahoi, E.G. Marin, T. Cusati, A. Fortunelli, G. Iannaccone, G. Fiori, M.C. Lemme, Ultralow Specific Contact Resistivity in Metal–Graphene Junctions via Contact Engineering, Adv. Mater. Interfaces 6 (2019) 1801285.

[53] T. O. Wehling, K. S. Novoselov, S. V. Morozov, E. E. Vdovin, M. I. Katsnelson, A. K.Geim, A. I. Lichtenstein, Molecular Doping of Graphene, Nano Lett. 8 (2008) 173-177.

[54] G. Froehlicher, S. Berciaud, Raman spectroscopy of electrochemically gated graphene transistors: Geometrical capacitance, electron-phonon, electron-electron, and electron-defect scattering, Phys. Rev. B - Condens. Matter Mater. Phys. 91 (2015) 1–17.

[55] A. Das, S. Pisana, B. Chakraborty, S. Piscanec, S.K. Saha, U. V. Waghmare, K.S. Novoselov, H.R. Krishnamurthy, A.K. Geim, A.C. Ferrari, A.K. Sood, Monitoring dopants by Raman scattering in an electrochemically top-gated graphene transistor, Nat. Nanotechnol. 3 (2008) 210–215.

[56] M. Kalbac, A. Reina-Cecco, H. Farhat, J. Kong, L. Kavan, M.S. Dresselhaus, The Influence of Strong Electron and Hole Doping on the Raman Intensity of, ACS Nano 4 (2010) 6055–6063.

[57] M. Jindra, M. Velický, M. Bouša, G. Abbas, M. Kalbáč, O. Frank, Localized Spectroelectrochemical Identification of Basal Plane and Defect-Related Charge-Transfer Processes in Graphene, J. Phys. Chem. Lett. 13 (2022) 642–648.

[58] M.M. Thackeray, C. Wolverton, E.D. Isaacs, Electrical energy storage for transportation - Approaching the limits of, and going beyond, lithium-ion batteries, Energy Environ. Sci. 5 (2012) 7854–7863.

[59] M.S. Dresselhaus, G. Dresselhaus, Intercalation compounds of graphite, Adv. Phys. 51

(2002) 1–186.

[60] I.A. Rodríguez-Pérez, X. Ji, Anion Hosting Cathodes in Dual-Ion Batteries, ACS Energy Lett. 2 (2017) 1762–1770.

[61] T. Placke, O. Fromm, S. Rothermel, G. Schmuelling, P. Meister, H.-W. Meyer, S. Passerini, M. Winter, Electrochemical Intercalation of Bis(Trifluoromethanesulfonyl) Imide Anion into Various Graphites for Dual-Ion Cells, ECS Trans. 50 (2013) 59–68.

[62] Y. Kondo, Y. Miyahara, T. Fukutsuka, K. Miyazaki, T. Abe, Electrochemical intercalation of bis(fluorosulfonyl)amide anions into graphite from aqueous solutions, Electrochem. Commun. 100 (2019) 26–29.

[63] D. Zhu, H. Wang, Hexafluorophosphate Anion Intercalation into Graphite Electrodes from Propylene Carbonate/Gamma-Butyrolactone Solutions, Langmuir 37 (2021) 10797–10805.

[64] Y. Wang, J. Li, Y. Huang, H. Wang, Anion Storage Behavior of Graphite Electrodes in LiBF4/Sulfone/Ethyl Methyl Carbonate Solutions, Langmuir 35 (2019) 14804–14811.

[65] Z. Lv, M. Han, J. Sun, L. Hou, H. Chen, Y. Li, M.C. Lin, A high discharge voltage dual-ion rechargeable battery using pure (DMPI+)(AlCl4−) ionic liquid electrolyte, J. Power Sources 418 (2019) 233–240.

[66] Z.A. Zafar, G. Abbas, K. Knizek, M. Silhavik, P. Kumar, P. Jiricek, J. Houdková, O. Frank, J. Cervenka, Chaotropic anion based “water-in-salt” electrolyte realizes a high voltage Zn-graphite dual-ion battery, J. Mater. Chem. A 10 (2022) 2064–2074.

[67] F. Bordet, K. Ahlbrecht, J. Tübke, J. Ufheil, T. Hoes, M. Oetken, M. Holzapfel, Anion intercalation into graphite from a sodium-containing electrolyte, Electrochim. Acta 174 (2015) 1317–1323.

[68] K. Xu, Electrolytes and interphases in Li-ion batteries and beyond, Chem. Rev. 114 (2014) 11503–11618.

[69] X. Jiang, L. Luo, F. Zhong, X. Feng, W. Chen, X. Ai, H. Yang, Y. Cao, Electrolytes for Dual-Carbon Batteries, ChemElectroChem 6 (2019) 2615–2629.

[70] P. Wang, Z. Chen, H. Wang, Z. Ji, Y. Feng, J. Wang, J. Liu, M. Hu, J. Fei, W. Gan, Y. Huang, A high-performance flexible aqueous Al ion rechargeable battery with long cycle life, Energy Storage Mater. 25 (2020) 426–435.

[71] S. Nandi, S.K. Das, Realizing a Low-Cost and Sustainable Rechargeable Aqueous Aluminum-Metal Battery with Exfoliated Graphite Cathode, ACS Sustain. Chem. Eng. 7 (2019) 19839–19847.

[72] Z. Liu, Y. Huang, Y. Huang, Q. Yang, X. Li, Z. Huang, C. Zhi, Voltage issue of aqueous rechargeable metal-ion batteries, Chem. Soc. Rev. 49 (2020) 180–232.

[73] T. Liang, R. Hou, Q. Dou, H. Zhang, X. Yan, The Applications of Water-in-Salt Electrolytes in Electrochemical Energy Storage Devices, Adv. Funct. Mater. 31 (2021) 2006749.

[74] Z.A. Zafar, G. Abbas, M. Silhavik, K. Knizek, O. Kaman, F.J. Sonia, P. Kumar, P. Jiricek, J. Houdková, O. Frank, J. Cervenka, Reversible anion intercalation into graphite from aluminum perchlorate “water-in-salt” electrolyte, Electrochim. Acta 404 (2022) 139754.

[75] J. Xu, Y. Dou, Z. Wei, J. Ma, Y. Deng, Y. Li, H. Liu, S. Dou, Recent Progress in Graphite Intercalation Compounds for Rechargeable Metal (Li, Na, K, Al)-Ion Batteries, Adv. Sci. 4 (2017) 1700146.

[76] G. Abbas, F.J. Sonia, Z.A. Zafar, K. Knížek, J. Houdková, P. Jiříček, M. Bouša, J. Plšek, M. Kalbáč, J. Červenka, O. Frank, Influence of structural properties on (de-)intercalation of ClO4− anion in graphite from concentrated aqueous electrolyte, Carbon 186 (2022) 612–623.

[77] K.L. Ng, M. Malik, E. Buch, T. Glossmann, A. Hintennach, G. Azimi, A low-cost rechargeable aluminum/natural graphite battery utilizing urea-based ionic liquid analog, Electrochim. Acta 327 (2019) 135031.

[78] C. Liu, Z. Liu, H. Niu, C. Wang, Z. Wang, B. Gao, J. Liu, M. Taylor, Preparation and in-situ Raman characterization of binder-free u-GF@CFC cathode for rechargeable aluminum-ion battery, MethodsX 6 (2019) 2374–2383.

[79] F. Kokai, R. Sorin, H. Chigusa, K. Hanai, A. Koshio, M. Ishihara, Y. Koga, M. Hasegawa, N. Imanishi, Y. Takeda, Ultrasonication fabrication of high quality multilayer graphene flakes and their characterization as anodes for lithium ion batteries, Diam. Relat. Mater. 29 (2012) 63–68.

[80] S. Kaewmala, W. Limphirat, V. Yordsri, H. Kim, S. Muhammad, W.S. Yoon, S. Srilomsak, P. Limthongkul, N. Meethong, Structural and Electrochemical Kinetic Properties of 0.5Li2MnO3·0.5LiCoO2 Cathode Materials with Different Li2MnO3 Domain Sizes, Sci. Rep. 9 (2019) 1–12.

[81] A. Heckmann, O. Fromm, U. Rodehorst, P. Münster, M. Winter, T. Placke, New insights into electrochemical anion intercalation into carbonaceous materials for dual-ion batteries: Impact of graphitization degree, Carbon 131 (2018) 201–212.

[82] J. Zou, C. Sole, N.E. Drewett, M. Velický, L.J. Hardwick, In Situ Study of Li Intercalation into Highly Crystalline Graphitic Flakes of Varying Thicknesses, J. Phys. Chem. Lett. 7 (2016) 4291–4296.

[83] N. Li, D. Su, In-situ structural characterizations of electrochemical intercalation of graphite compounds, Carbon Energy 1 (2019) 200–218.

[84] S. Oswald, K. Nikolowski, H. Ehrenberg, Quasi in situ XPS investigations on intercalation mechanisms in Li-ion battery materials, Anal. Bioanal. Chem. 393 (2009) 1871–1877.

[85] Y. Zhang, F. Lu, L. Pan, Y. Xu, Y. Yang, Y. Bando, D. Golberg, J. Yao, X. Wang, Improved cycling stability of NiS2 cathodes through designing a “kiwano” hollow structure, J. Mater. Chem. A 6 (2018) 11978–11984.

[86] H. Fan, L. Qi, H. Wang, Intercalation Behavior of Hexafluorophosphate into Graphite Electrode from Propylene/Ethylmethyl Carbonates, J. Electrochem. Soc. 164 (2017) A2262–A2267.

[87] B. Wang, Y. Wang, Y. Huang, L. Zhang, S. Ma, H. Wang, Hexafluorophosphate Intercalation into the Graphite Electrode from Mixed Cyclic Carbonates, ACS Appl. Energy Mater. 4 (2021) 5316–5325.

[88] M. Kalbac, A. Reina-Cecco, H. Farhat, J. Kong, L. Kavan, M.S. Dresselhaus, The influence of strong electron and hole doping on the Raman intensity of chemical vapor-deposition graphene, ACS Nano 4 (2010) 6055–6063.

[89] Z. Komínková, M. Kalbáč, Electrochemical charging of the single-layer graphene membrane, Phys. Status Solidi Basic Res. 253 (2016) 2331–2335.

[90] L. Zou, B. Huang, Y. Huang, Q. Huang, C. Wang, An investigation of heterogeneity of the degree of graphitization in carbon-carbon composites, Mater. Chem. Phys. 82 (2003) 654–662.

[91] K. Akikubo, T. Kurahashi, S. Kawaguchi, M. Tachibana, Thermal expansion measurements of nano-graphite using high-temperature X-ray diffraction, Carbon 169 (2020) 307–311.

[92] N. Iwashita, X-ray Powder Diffraction, Materials Science and Engineering of Carbon, Butterworth-Heinemann (2016) 7–25.

[93] A. Jorio, E.H. Martins Ferreira, L. G., C. A., R. B., Measuring Disorder in Graphene with Raman Spectroscopy, Phys. Appl. Graphene, Intechopen (2011) 440–454.

[94] J. Gao, S. Tian, L. Qi, H. Wang, Intercalation manners of perchlorate anion into graphite electrode from organic solutions, Electrochim. Acta 176 (2015) 22–27.

[95] A. Ejigu, L. Le, K. Fujisawa, M. Terrones, J. Andrew, J.Forsyth, R. Dryfe, Electrochemically Exfoliated Graphene Electrode for High Performance Rechargeable Chloroaluminate and Dual ion Batteries, ACS Appl. Mater. Interfaces 11 (2019) 23261–23270.

[96] M. Angell, C.J. Pan, Y. Rong, C. Yuan, M.C. Lin, B.J. Hwang, H. Dai, High Coulombic efficiency aluminum-ion battery using an AlCl3-urea ionic liquid analog electrolyte, Proc. Natl. Acad. Sci. U. S. A. 114 (2017) 834–839.

[97] S. Tian, L. Qi, H. Wang, Difluoro(oxalato)borate anion intercalation into graphite electrode from ethylene carbonate, Solid State Ionics 291 (2016) 42–46.

[98] F.J. Sonia, M.K. Jangid, B. Ananthoju, M. Aslam, P. Johari, A. Mukhopadhyay,

Understanding the Li-storage in few layers graphene with respect to bulk graphite: Experimental, analytical and computational study, J. Mater. Chem. A 5 (2017) 8662–8679.

[99] F.J. Sonia, M.K. Jangid, M. Aslam, P. Johari, A. Mukhopadhyay, Enhanced and faster potassium storage in graphene with respect to graphite: A comparative study with lithium storage, ACS Nano 13 (2019) 2190–2204.

[100] M.K. Jangid, A.S. Lakhnot, A. Vemulapally, F.J. Sonia, S. Sinha, R.O. Dusane, A. Mukhopadhyay, Crystalline core/amorphous shell structured silicon nanowires offer size and structure dependent reversible Na-storage, J. Mater. Chem. A 6 (2018) 3422–3434.

[101] E. Flores, P. Novák, E.J. Berg, In situ and Operando Raman spectroscopy of layered transition metal oxides for Li-ion battery cathodes, Front. Energy Res. 6 (2018) 1–16.

[102] C.J. Pan, C. Yuan, G. Zhu, Q. Zhang, C.J. Huang, M.C. Lin, M. Angell, B.J. Hwang, P. Kaghazchi, H. Dai, An operando X-ray diffraction study of chloroaluminate anion-graphite intercalation in aluminum batteries, Proc. Natl. Acad. Sci. U. S. A. 115 (2018) 5670–5675.

[103] G. Schmuelling, T. Placke, R. Kloepsch, O. Fromm, H.W. Meyer, S. Passerini, M. Winter, X-ray diffraction studies of the electrochemical intercalation of bis(trifluoromethanesulfonyl)imide anions into graphite for dual-ion cells, J. Power Sources 239 (2013) 563–571.

[104] D. Zhu, H. Fan, H. Wang, PF 6-Intercalation into Graphite Electrode from Propylene Carbonate, ACS Appl. Energy Mater. 4 (2021) 2181-2189.

# 6 Complete list of publications

1. **G. Abbas**, F.J. Sonia, Z.A. Zafar, K. Knížek, J. Houdková, P. Jiříček, M. Bouša, J. Plšek, M. Kalbáč, J. Červenka, O. Frank, Influence of structural properties on (de-)intercalation of $ClO_4^-$ anion in graphite from concentrated aqueous electrolyte, *Carbon* 186 (2022) 612–623.

2. **G. Abbas**, Z.A. Zafar, F.J. Sonia, J. Houdková, P. Jiříček, M. Kalbáč, J. Cervenka and O. Frank, The Effects of Ultrasound Treatment of Graphite on the Reversibility of (De)intercalation of Anion from Aqueous Electrolyte Solution, *Nanomaterials* 12 (2022) 3932.

3. Z.A. Zafar, **G. Abbas**, M. Silhavik, K. Knizek, O. Kaman, F.J. Sonia, P. Kumar, P. Jiricek, J. Houdková, O. Frank, J. Cervenka, Reversible anion intercalation into graphite from aluminum perchlorate "water-in-salt" electrolyte, *Electrochim. Acta* 404 (2022) 139754.

4. Z.A. Zafar, **G. Abbas**, K. Knizek, M. Silhavik, P. Kumar, P. Jiricek, J. Houdková, O. Frank, J. Cervenka, Chaotropic anion based "water-in-salt" electrolyte realizes a high voltage Zn-graphite dual-ion battery, *J. Mater. Chem. A* 10 (2022) 2064–2074.

5. M. Jindra, M. Velický, M. Bouša, **G. Abbas**, M. Kalbáč, and O. Frank, Localized Spectroelectrochemical Identification of Basal Plane and Defect-Related Charge-Transfer Processes in Graphene, *J. Phys. Chem. Lett*. 13 (2022) 642−648.

6. R. Razaq, D. Sun, J. Wang, Y. Xin, **G. Abbas**, J. Zhang, Q. Li, T. Huang, Z. Zhang, Y. Huang, Ultrahigh sulfur loading in $ZnS_{1-x}$ / rGO through in situ oxidation-refilling route for high-performance Li–S batteries, *J. Power Sources* 414, (2019) 453-459.

7. M. Arshad, A. Qayyum, **G. Abbas**, R. Haider, M. Iqbal, A. Nazir, Influence of different solvents on portrayal and photocatalytic activity of tin-doped zinc oxide nanoparticles, *J. Mol. Liq*. 260 (2018) 272–278.

8. **G. Abbas**, S. Asim, H.N. Bhatti, A. Mansha, M. Zahid, M. Ahmad, R. Haider, Spectroscopic studies of interactions of 2-(2-Oxo-2-Phenylethyl)-1, 2-benzisothiazol-3(2H)-one-1, 1-dioxide with human DNA, *J. Mol. Struct*. 1196 (2019) 403–408.

9. M. Ahmad, **G. Abbas**, R. Haider, F. Jalal, G.A. Shar, G.A. Soomro, N. Qureshi, M. Iqbal, A. Nazir, Kinetics and Equilibrium Studies of Eriobotrya Japonica: A Novel Adsorbent Preparation for Dyes Sequestration, *Zeitschrift Fur Phys. Chemie*. 233 (2019), 1469-1484.

10. **G. Abbas**, I. Javed, M. Iqbal, R. Haider, F. Hussain, N. Qureshi, Adsorption of non-steroidal anti-inflammatory drugs (Diclofenac and ibuprofen) from aqueous medium onto activated onion skin, *Desalin. Water Treat.* 95 (2017) 274–285.

## 6.1 Publications in preparation

1. **G. Abbas**, F. J. Sonia, M. Jindra, J. Cervenka, M. Kalbáč, O. Frank and M. Velický, Electrostatic doping of graphene using concentrated aqueous electrolytes of differing ionic strength, (*draft prepared)*.

2. **G. Abbas**, M. Kalbáč, O. Frank and M. Velický, Charge induced doping in oxygen plasma treated graphene using the concentrated aqueous electrolyte, (*in preparation)*.

3. **G. Abbas**, M. Kalbáč, O. Frank and M. Velický, Role of defects for charge transfer in functionalized monolayer graphene by using concentrated aqueous electrolytes, (*in preparation)*.

4. **G. Abbas**, Z.A. Zafar, F.J. Sonia, M. Kalbáč, J. Cervenka and O. Frank, Investigations for the structural stability of $VO_x$-rGO nanorods as binder free anode material for Lithium ion batteries, (*draft prepared)*.

5. **G. Abbas**, Z.A. Zafar, F.J. Sonia, M. Kalbáč, J. Cervenka and O. Frank, Influence of structural morphology of $MoS_2$ encapsulated in N-doped Carbon sphere as anode material for Li ion batteries, (*in preparation)*.

6. **G. Abbas**, Z.A. Zafar, F.J. Sonia, O. Frank and J. Červenka, Recent advances for cathode materials in Rechargeable Al ion batteries: An electrochemistry perspective, (*draft prepared)*.

## 6.2 Conference proceedings:

1. **G. Abbas**, F.J. Sonia, M. Velický, M. Kalbáč and O. Frank, In-Situ Raman Spectroelectrochemical Doping of Monolayer Graphene at Micro-Scale, MA2021-02(49):1445-1445, ECS, *Meet. Abstr.* MA2021−023.

2. Z.A. Zafar, K. Knizek, **G. Abbas**, M. Silhavik, and J. Cervenka, Perchlorate Based "Water-in-Salt" Electrolyte for Electrochemical Energy Storage Systems, ECS, *Meet. Abstr.* MA2021−023.

3. Z.A. Zafar, **G. Abbas**, M. Silhavik and J. Cervenka "Water-in-Salt" Electrolyte Promises Reversible Anion Intercalation into Graphite for Energy Storage Applications *Meet. Abstr.* MA2020−02 3794.

# 7 Abbreviations

| Abbreviation | Name |
|---|---|
| 1-L | Monolayer |
| 2DMs | Two dimensional materials |
| CVD | Chemical vapor deposition |
| NG | Natural graphite |
| KG | Kish graphite |
| HOPG | Highly oriented pyrolytic graphite |
| WE | Working electrode |
| SEC | Spectroelectrochemistry |
| CV | Cyclic voltammetry |
| NMP | *N*-methyl-2-pyrrolidone |
| PVDF | Polyvinylidene fluoride |
| XRD | X-ray diffraction |
| SEM | Scanning electron microscopy |
| XPS | X-Ray photoelectron spectroscopy |
| FTIR-ATR | Fourier transform infrared spectroscopy-Attenuated total reflection |

# 8 List of Appendices

1) M. Jindra, M. Velický, M. Bouša, **G. Abbas**, M. Kalbáč, O. Frank, Localized Spectroelectrochemical Identification of Basal Plane and Defect-Related Charge-Transfer Processes in Graphene, *J. Phys. Chem. Lett.* 13 (2022) 642–648.

2) **G. Abbas**, F.J. Sonia, Z.A. Zafar, K. Knížek, J. Houdková, P. Jiříček, M. Bouša, J. Plšek, M. Kalbáč, J. Červenka , O. Frank, Influence of structural properties on (de-)intercalation of $ClO_4^-$ anion in graphite from concentrated aqueous electrolyte, *Carbon* 186 (2022) 612–623.

3) **G. Abbas**, , Z.A. Zafar, F.J. Sonia K. Knížek, J. Houdková, P. Jiříček, M. Kalbáč, J. Červenka , O. Frank, The Effects of Ultrasound Treatment of Graphite on the Reversibility of (De)intercalation of Anion from Aqueous Electrolyte Solution, *Nanomaterials* 12 (2022) 3932.

4) Z.A. Zafar, **G. Abbas**, M. Silhavik, K. Knizek, O. Kaman, F.J. Sonia, P. Kumar, P. Jiricek, J. Houdková, O. Frank, J. Cervenka, Reversible anion intercalation into graphite from aluminum perchlorate “water-in-salt” electrolyte, *Electrochim. Acta* 404 (2022) 139754.

## 8.1 Appendix 1

M. Jindra, M. Velický, M. Bouša, **G. Abbas**, M. Kalbáč, O. Frank, Localized Spectroelectrochemical Identification of Basal Plane and Defect-Related Charge-Transfer Processes in Graphene, *J. Phys. Chem. Lett*. 13 (2022) 642–648.

## 8.2 Appendix 2

**G. Abbas**, F.J. Sonia, Z.A. Zafar, K. Knížek, J. Houdková, P. Jiříček, M. Bouša, J. Plšek, M. Kalbáč, J. Červenka , O. Frank, Influence of structural properties on (de-)intercalation of $ClO_4^-$ anion in graphite from concentrated aqueous electrolyte, *Carbon* 186 (2022) 612–623.

## 8.3 Appendix 3

**G. Abbas**, Z.A. Zafar, F.J. Sonia K. Knížek, J. Houdková, P. Jiříček, M. Kalbáč, J. Červenka , O. Frank, The Effects of Ultrasound Treatment of Graphite on the Reversibility of (De)intercalation of Anion from Aqueous Electrolyte Solution, *Nanomaterials* 12 (2022) 3932.

## 8.4 Appendix 4

Z.A. Zafar, **G. Abbas**, M. Silhavik, K. Knizek, O. Kaman, F.J. Sonia, P. Kumar, P. Jiricek, J. Houdková, O. Frank, J. Cervenka, Reversible anion intercalation into graphite from aluminum perchlorate “water-in-salt” electrolyte, *Electrochim. Acta* 404 (2022) 139754.